

Spin-enhanced nanodiamond biosensing for ultrasensitive diagnostics

<https://doi.org/10.1038/s41586-020-2917-1>

Received: 24 May 2019

Accepted: 16 September 2020

Published online: 25 November 2020

 Check for updates

Benjamin S. Miller^{1,2✉}, Léonard Bezingé¹, Harriet D. Gliddon¹, Da Huang¹, Gavin Dold^{1,3}, Eleanor R. Gray¹, Judith Heaney⁴, Peter J. Dobson⁵, Eleni Nastouli⁶, John J. L. Morton^{1,3} & Rachel A. McKendry^{1,2✉}

The quantum spin properties of nitrogen-vacancy defects in diamond enable diverse applications in quantum computing and communications¹. However, fluorescent nanodiamonds also have attractive properties for in vitro biosensing, including brightness², low cost³ and selective manipulation of their emission⁴. Nanoparticle-based biosensors are essential for the early detection of disease, but they often lack the required sensitivity. Here we investigate fluorescent nanodiamonds as an ultrasensitive label for in vitro diagnostics, using a microwave field to modulate emission intensity⁵ and frequency-domain analysis⁶ to separate the signal from background autofluorescence⁷, which typically limits sensitivity. Focusing on the widely used, low-cost lateral flow format as an exemplar, we achieve a detection limit of 8.2×10^{-19} molar for a biotin–avidin model, 10^5 times more sensitive than that obtained using gold nanoparticles. Single-copy detection of HIV-1 RNA can be achieved with the addition of a 10-minute isothermal amplification step, and is further demonstrated using a clinical plasma sample with an extraction step. This ultrasensitive quantum diagnostics platform is applicable to numerous diagnostic test formats and diseases, and has the potential to transform early diagnosis of disease for the benefit of patients and populations.

Fluorescent nanodiamonds (FNDs) that contain nitrogen-vacancy (NV) centres—defects that have optical transitions within the band-gap—have received considerable attention as a spin system for use as a qubit in quantum computing and communication, and for quantum sensing^{1,4,8,9}. Such applications arise from the ability of the negative NV (NV⁻) centre spin state to be optically initialized and read out, while being manipulated using direct current and microwave magnetic fields. FNDs also have attractive fluorescent properties—including a high quantum yield and a lack of blinking and photobleaching—as well as high stability, low cytotoxicity^{2,10}, the availability of surface groups for bio-functionalization¹¹, and ease of mass manufacture, such as by the milling of high-pressure, high-temperature diamond^{3,12}. The sensing applications of NV centres⁴ include magnetic field quantification^{13–15}, temperature sensing^{16,17} and biological labelling^{2,18}, the latter of which includes cellular imaging¹⁹, drug delivery²⁰ and contrast enhancement in magnetic resonance imaging²¹. A key advantage of NV⁻ centres is that, unlike neutral (NV⁰) centres, their fluorescence can be selectively modulated by spin manipulation⁴, which enables signal separation for imaging in high-background environments. This property has been used to improve the contrast for imaging by modulating the fluorescence with microwaves^{5,22}, magnetic fields^{23,24} or near-infrared light²⁵. Here we investigate the use of FNDs for in vitro diagnostics.

Communicable diseases represent an enormous global health challenge, and disproportionately affect poorer populations with limited

access to healthcare²⁶. At the end of 2015, there were 36.9 million people living with HIV worldwide, of whom 9.4 million (25%) were unaware of their HIV status²⁷. Early diagnosis is crucial for effective treatment and prevention and benefits patients and populations. For example, patients in the UK that started antiretroviral therapy for HIV after a late diagnosis had a reduction in life expectancy of more than 12 years compared with those that started treatment after an earlier diagnosis²⁸. The earliest marker of HIV is viral RNA, which is detectable 7 days before antigen and 16 days before antibodies²⁹. Point-of-care nucleic acid testing therefore offers the potential for diagnosis at an earlier stage than either existing laboratory-based nucleic acid tests or point-of-care protein tests.

Rapid point-of-care tests have transformed access to disease testing in various community settings, including clinics, pharmacies and the home³⁰. Among the most frequently used tests worldwide are paper microfluidic lateral flow assays (LFAs), of which 276 million were sold in 2017 for malaria alone³¹. LFAs satisfy many of the REASSURED criteria³² for diagnostics; however, despite their widespread use, they are still limited by inadequate sensitivity to the low levels of biomarkers present in early disease.

Fluorescent markers can be highly sensitive, but their practical application is limited by background fluorescence from the sample, the substrate or the readout technique. In the case of nitrocellulose substrates used in LFAs, there is a considerable background

¹London Centre for Nanotechnology, University College London, London, UK. ²Division of Medicine, University College London, London, UK. ³Department of Electronic and Electrical Engineering, University College London, London, UK. ⁴Advanced Pathogens Diagnostic Unit, University College London Hospitals, London, UK. ⁵The Queens College, University of Oxford, Oxford, UK. ⁶Department of Virology, University College London Hospitals, London, UK. ✉e-mail: ben.miller.13@ucl.ac.uk; r.a.mckendry@ucl.ac.uk

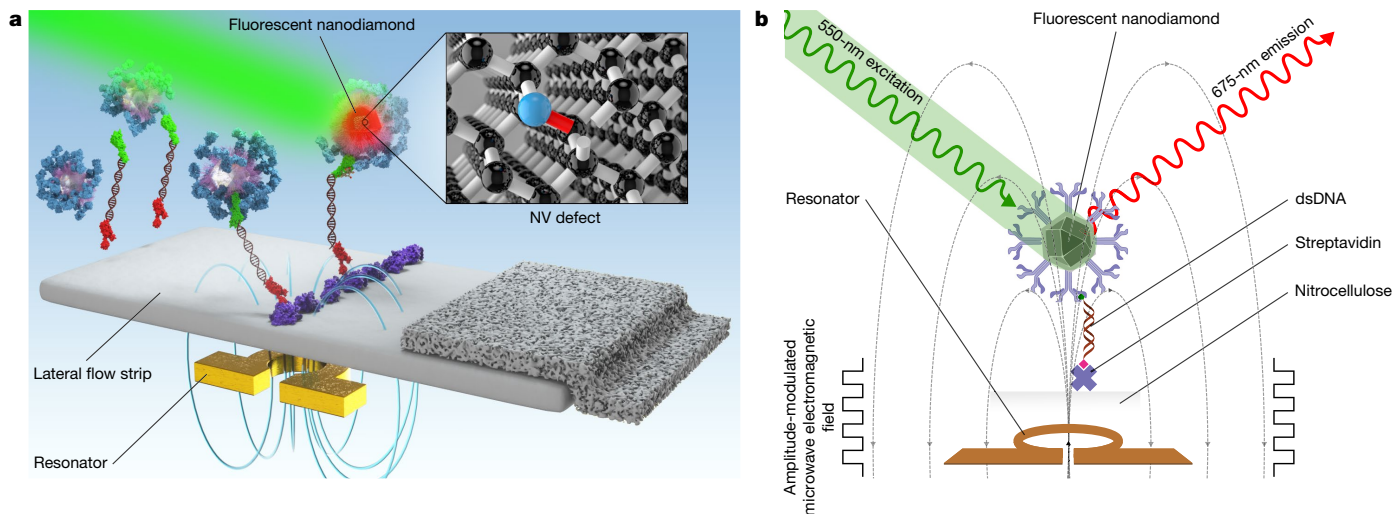


Fig. 1 | Schematic illustration of the use of FNDs in LFAs. **a**, Illustration of the concept of using FNDs in an LFA. The binding of DNA modifications causes FNDs to be immobilized at the test line in a sandwich-format LFA. The inset shows the atomic structure of an NV⁻ centre, the origin of FND fluorescence. An omega-shaped stripline resonator applies a microwave field over the LFA, modulating the fluorescence intensity. **b**, Schematic showing more detail of the principle. FNDs are immobilized at the test line in a sandwich structure in

the presence of double-stranded DNA (dsDNA) amplicons. Exciting at 550 nm (green) produces fluorescence emission centred at 675 nm (red), imaged with a camera. An amplitude-modulated microwave field, applied by the resonator, selectively modulates the fluorescence of the immobilized FNDs at a set frequency. This enables specific separation of the FND fluorescence from background fluorescence in the frequency domain, to improve the signal-to-noise ratio.

autofluorescence⁷, which inherently limits sensitivity. Various methods have been reported to reduce this effect, such as membrane modification to reduce background fluorescence³³, exciting in the near-infrared range and using upconverting nanoparticles³⁴, and time-gated detection using long-persistent phosphors³⁵ to separate out the shorter-lived background fluorescence. The use of these methods has led to improvements in sensitivity of approximately 10-fold compared with gold nanoparticles, but they are limited by relatively low brightness.

Here we show the use of FNDs as a fluorescent label in an LFA format, demonstrating their first—to our knowledge—use for in vitro diagnostics. This strategy takes advantage of the high brightness and selective modulation of FNDs, and the use of a narrowband resonator enables the low-power generation of microwave-frequency electromagnetic fields—suitable for a point-of-care device—that can efficiently separate the signal from the background in the frequency domain by lock-in⁶ detection. After characterization, functionalization and optimization, we applied FND-based LFAs first to a model system and then to a molecular HIV-1 RNA assay in order to demonstrate their clinical utility.

Microwave modulation of FND emission on paper

An illustration of the use of FNDs in LFAs is shown in Fig. 1. FNDs can be used as nanoparticle labels on nitrocellulose strips, on which they undergo a multiple-step binding assay with little user input to bind at the test line in the presence of the target nucleic acids. After immobilization, the fluorescence of the FNDs can be modulated at a fixed frequency using a microwave field, enabling them to be specifically detected and quantified.

Figure 2a shows an energy-level diagram of the NV⁻ centre, which is the origin of FND fluorescence. The triplet ground state is optically driven into an excited triplet state, which then undergoes radiative decay back to the ground states. Throughout the process, the electron spin state ($m_s = 0, \pm 1$) is conserved; however, the $m_s = \pm 1$ excited-state levels can decay into a metastable ‘dark’ state with a corresponding reduction in fluorescence⁴. Resonant microwave radiation drives electron spin population from the $m_s = 0$ to the $m_s = \pm 1$ levels, reducing the intensity of the fluorescence. The microwave field was produced by a voltage-controlled oscillator connected to an antenna, capacitively

coupled to an omega-shaped stripline resonator that provides a uniform peak field over the measurement area (the area of the resonator).

The fluorescence of the FNDs, and its response to the microwave field, was measured on the nitrocellulose paper substrate. To investigate the fluorescence intensity as a function of microwave frequency on paper, a wideband resonator was used to perform continuous-wave electron spin resonance spectroscopy, as shown in Extended Data Fig. 1a–c. A plot of FND fluorescence over a wide frequency range is shown in Fig. 2b, showing two peaks at $\Delta E = 2.87$ GHz and $\Delta E^* = 1.43$ GHz, corresponding to the triplet level splitting in the ground and excited states, respectively. Figure 2c shows a narrowband resonator (characterized in Extended Data Fig. 1d–f) that is designed to have a resonant frequency at 2.87 GHz with quality factor $Q = 100$; this induced a reduction in measured fluorescence of around 3–6% (Extended Data Fig. 1f), which varied linearly with the microwave input power in dBm (see Extended Data Fig. 1g, h).

The excitation and emission spectra of FNDs are shown in Fig. 2d. The presence of NV⁻ centres is indicated by the zero-phonon line at around 640 nm. Using an amplitude-modulated microwave field to specifically vary the FND fluorescence at a fixed frequency enables the application of a computational lock-in algorithm⁶ (shown schematically in Extended Data Fig. 2a) to selectively extract signals at the reference frequency. This lock-in analysis, shown in ref. ⁵, separates the periodic FND fluorescence from the non-periodic background fluorescence (the autofluorescence of nitrocellulose), thus improving sensitivity.

The fluorescence modulation is shown in Fig. 2e, f. Figure 2e shows pixel variation over time: the test line, on which FNDs are immobilized, has a high variance compared to the background, which does not modulate and has low variance. The time series is shown in Fig. 2f (top), in which a square-wave 4 Hz amplitude-modulated microwave field modulates the fluorescence intensity. Application of the lock-in algorithm over a small frequency range gave the plot in Fig. 2f (bottom)—an absolute sinc function, the Fourier transform of a square pulse. The maximum response is shown when the reference frequency matches the modulation frequency at 4 Hz. The optimization of modulation frequency, sampling frequency, exposure time and measurement time are shown in Extended Data Fig. 2b–e. Microwave generation was miniaturized using a voltage-controlled oscillator, amplifier, and

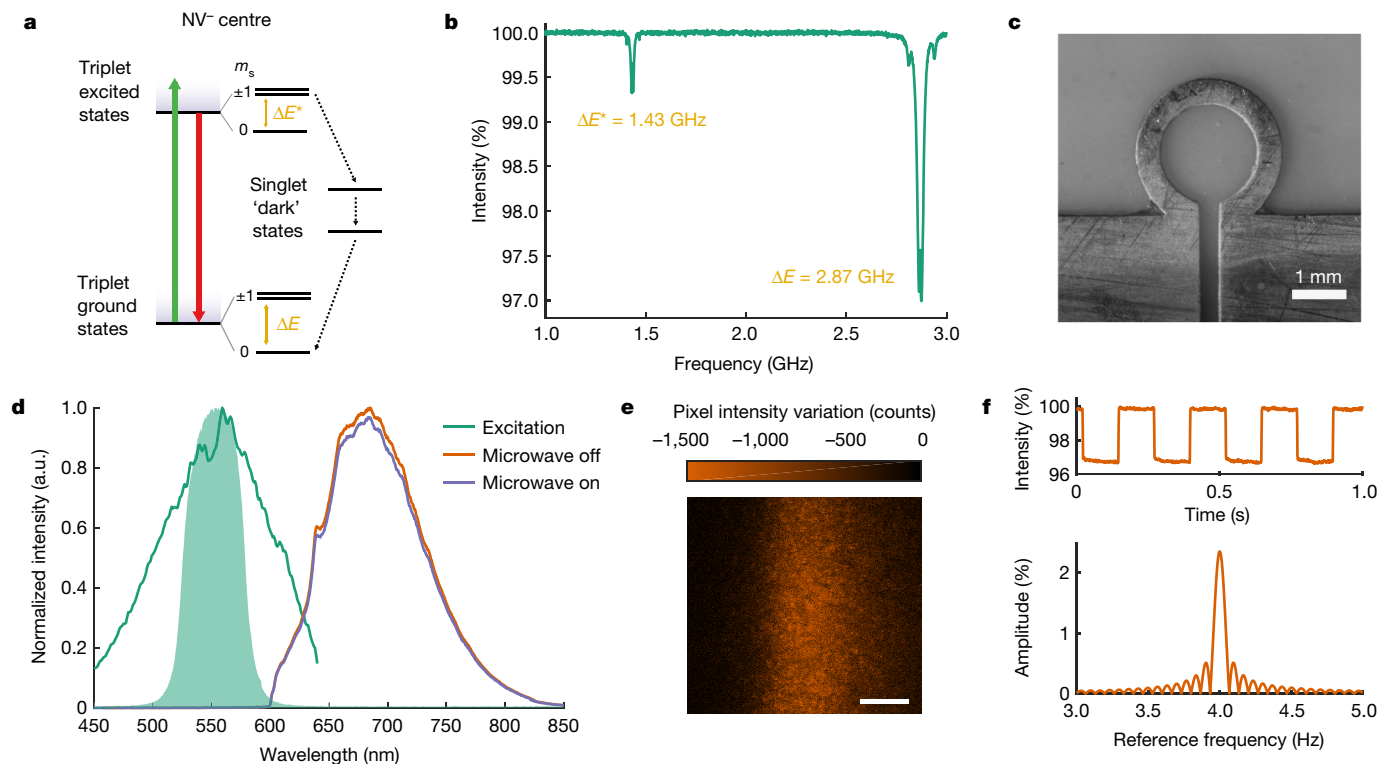


Fig. 2 | Microwave modulation of FNDs on paper. **a**, Energy-level diagram of an NV⁻ centre. Splitting in the ground and excited states is labelled as ΔE and ΔE^* , respectively. **b**, The variation in FND fluorescence under microwave fields of different frequency, showing dips at energies ΔE and ΔE^* . Some peak splitting is observed around the centre frequency due to a magnetic field of approximately 3 G generated by the resonator (measured with a Gaussmeter). **c**, A microscope image of the omega-shaped stripline resonator used to produce a uniform field at 2.87 GHz. **d**, Excitation and emission spectra of

FNDs. The green shaded area shows the filtered excitation light used. The area of the emission spectrum is reduced under the application of the microwave field. **e**, The pixel variation at the test line (with immobilized FNDs) of an LFA strip under an amplitude-modulated microwave field. **f**, Top, the variation of mean fluorescence intensity over time under the application of the same amplitude-modulated field. Bottom, applying a lock-in algorithm over a range of frequencies gives a sinc function with a peak at the modulation frequency. a.u., arbitrary units.

a custom power and timing circuit that measured 65 mm × 38 mm (Extended Data Fig. 2f, g).

Fundamental limits using a biotin–avidin model

After fluorescence characterization and optimization of the modulation parameters, FNDs were functionalized with biomolecules for incorporation into LFAs. We used FNDs with a hydrophilic polyglycerol layer in order to reduce non-specific binding to the nitrocellulose³⁶ (Extended Data Fig. 3a), a key factor that limits LFA sensitivity. Three sizes of FND–polyglycerol (characterized by dynamic light scattering, as shown in Extended Data Fig. 3b) were functionalized with antibodies via the activation of the alcohol groups of polyglycerol with disuccinimidyl carbonate³⁷, as shown in Extended Data Fig. 3c. Characterization by scanning electron microscopy, dynamic light scattering and Fourier transform infrared spectroscopy (Extended Data Fig. 3d–i) showed successful conjugation, with minimal aggregation upon functionalization and increases in size that were consistent with the size of the conjugants^{38,39}. The number of active binding sites on the surface of 600-nm-diameter FNDs was subsequently quantified using quantitative polymerase chain reaction (qPCR; Methods, Extended Data Fig. 4). The measured value of 4,300 active binding sites per FND is consistent with geometric calculations of the number of antibodies that could bind.

The fundamental limit of detection (LOD) of FND-based LFAs was investigated using a model biotin–avidin interaction. A serial dilution of a bovine serum albumin (BSA)–biotin–functionalized FND suspension was run on LFA strips, on which the FNDs bound directly to a printed poly-streptavidin test line (rather than in a sandwich formation) as

shown schematically in Fig. 3a. The high-affinity interaction between biotin and streptavidin, as well as the flow rate and the high binding capacity of nitrocellulose, ensures that the residency time of the FNDs at the test line is much longer than the binding time of biotinylated FNDs to the streptavidin (Extended Data Fig. 5a, b). This implies that all FNDs bind at the test line, making it ideal for benchmarking the best-case sensitivity and comparing with other nanomaterials. The LODs were quantified for FNDs with three different particle-core diameters: 120, 200 and 600 nm.

The resulting fluorescence signals from the LFA test line were analysed using lock-in analysis and conventional intensity analysis, in which the difference in fluorescence intensity between the test line and the background is measured. The results were compared with those of gold nanoparticles, which are frequently used in LFAs⁴⁰. The signal-to-blank ratios (SBRs) were plotted against the concentration of 600-nm FNDs (Fig. 3b). Each dilution series was fitted to a simple linear regression, and the LOD was defined as the intersection of the lower 95% confidence interval of the linear fit with the upper 95% confidence interval of the blanks⁴¹. Figure 3c shows images of the test lines as well as time series of the fluorescence modulation at each FND concentration, demonstrating that signal modulation can be measured well below the concentration at which there is a visible test line.

LODs were found to be 200 aM, 46 aM and 820 zM for particles of 120, 200 and 600 nm in diameter, respectively (Extended Data Fig. 5d). The best LODs were found with the larger particles, because the lock-in amplitude scales with the fluorescence modulation intensity, which in turn scales with the number of NV⁻ centres. The number of NV⁻ centres per particle scales with the volume, so the LOD should scale with the

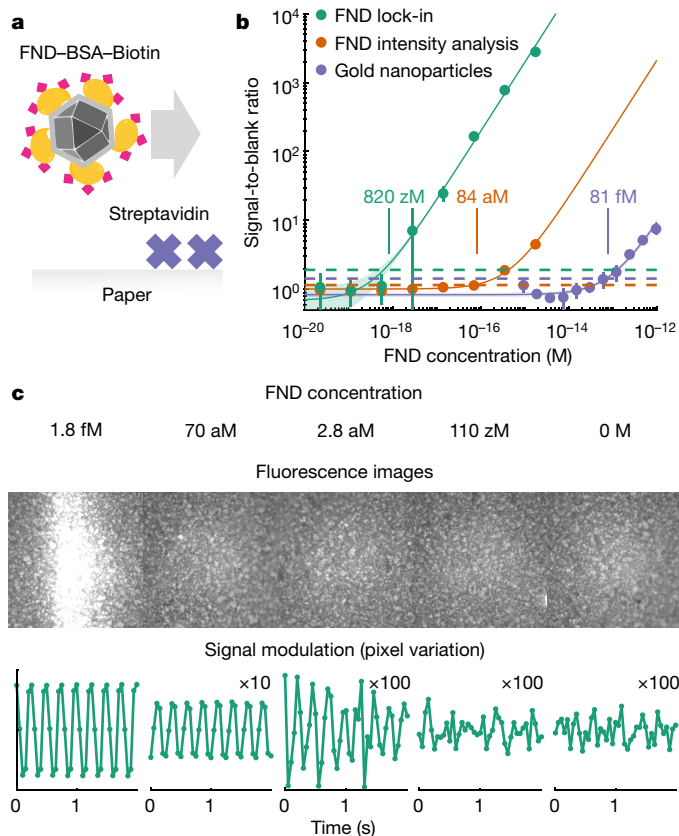


Fig. 3 | Characterizing the fundamental limit of detection using biotin-avidin binding of FNDs on LFAs. **a**, Schematic of the assay. FNDs functionalized with BSA-biotin were run on streptavidin-printed LFA strips, on which they bound directly to the test line. The arrow shows the flow direction. **b**, The SBRs of a dilution series of 600-nm FNDs were measured by both lock-in analysis and conventional intensity analysis, and compared to that of 50-nm gold nanoparticles. LODs were 820 zM, 83 aM and 81 fM, respectively. Lock-in analysis provided a 100-fold improvement over conventional intensity analysis, and a 98,000-fold improvement over gold nanoparticles. Dots show the means and error bars show s.d. of $n = 3$ technical replicates and $n = 3$ measurement replicates for each sample. **c**, An illustration of the comparison between lock-in and conventional analysis. Top, example fluorescence images at various concentrations; bottom, intensity-time plots, showing that a periodic signal is still evident after the test line is no longer visible in the images.

cube of the diameter. Additionally, surface effects reduce the fluorescence of NV^- centres close to the surface, so a larger volume-to-surface ratio should increase fluorescence intensity.

LODs using 600-nm FNDs were 820 zM and 83 aM using lock-in and conventional analysis, respectively, indicating that lock-in analysis yields a 620-fold improvement in the signal-to-background ratio and a 100-fold improvement in the LOD. This increases to an 810-fold improvement in signal-to-background ratio using 120-nm FNDs, giving a 380-fold improvement in the LOD.

This fundamental LOD of 820 zM corresponds to 0.5 particles per μl , or just 27 particles in a 55- μl sample. For comparison, the same experiment was performed with 50-nm gold nanoparticle labels, which are frequently used in LFAs⁴⁰ owing to their ease of functionalization and strong light absorption. The 600-nm FNDs were five orders of magnitude more sensitive than gold nanoparticles. The size of gold nanoparticles that can be used on LFAs is also limited by the broadening of the plasmonic peak, whereas FNDs at larger sizes become brighter. Owing to the low numbers of particles detected, the LODs of biological assays are expected to be limited by non-specific binding and equilibrium considerations, rather than by the fundamental sensitivity of FNDs.

Single-copy detection of HIV-1 RNA

This platform was then applied to a proof-of-concept assay for the detection of DNA amplicons. The assay is based on a reverse transcriptase-recombinase polymerase amplification (RT-RPA) reaction for the detection of HIV-1 RNA, which is performed with modified primers to form a sandwich structure on the nitrocellulose (Fig. 4a). After assay optimization (Methods, Extended Data Figs. 6–8), LFAs were performed with serial dilutions of RT-RPA products using FNDs of three particle sizes (120, 200 and 600 nm). The initial aim was to determine the sensitivity of the detection system, rather than the amplification step, so the amplicon concentration used was measured post-amplification. The resulting plots of SBR against amplicon concentration are shown in Fig. 4b, and fitted to the Langmuir adsorption isotherm model (equation (6), Methods). The LODs were measured as 9.0, 7.5 and 3.7 fM for 120, 200 and 600-nm FNDs, respectively. The LOD of 3.7 fM, achieved with 600-nm FNDs, corresponds to 2,200 copies per μl , or 1.1×10^5 copies in total (190 zmol of DNA).

A model ‘amplicon’ (described in Methods and characterized in Extended Data Fig. 9a, b) was used to compare the 600-nm FNDs with 40-nm gold nanoparticles. The resulting LODs, plotted in Extended Data Fig. 9c, show that FNDs provide an approximately 7,500-fold improvement over 40-nm gold nanoparticles. The approximately 13-fold reduction in improvement over gold nanoparticles compared to that found for the biotin-avidin model is due to non-specific binding. The blanks in the DNA assay have the same FND concentration as the positives, whereas in the biotin-avidin assay they are ‘true blanks’ (running buffer only). The resulting small lock-in amplitude in the blanks is around 13-fold higher than a ‘true blank’ signal (noise), showing no significant difference from the blanks from the biotin-avidin assay multiplied by this factor of 13 (two-tailed t -test, $P = 0.33$).

Achieving this level of sensitivity from FND labelling means that a short amplification step before addition of the sample to the LFA could lead to single-copy detection, with typical amplification factors⁴² for isothermal RPA of 10^4 in 10 min. This was subsequently demonstrated by performing 10 min (37 °C) RT-RPA reactions on serial dilutions of HIV-1 transcript RNA, before adding a 6 \times running buffer solution to the purified products and running on LFAs as previously. The resulting SBRs are plotted against RNA input copy number in Fig. 4c, showing a LOD of 1 copy. Positive results were achieved down to a single RNA copy. Statistical analysis of the lock-in amplitudes (analysis of variance) is shown in Extended Data Fig. 10a–c. Owing to the 10-min amplification time, all concentrations of at least 1 copy reach the saturation signal, so a qualitative yes/no result is given. The variation of SBR with amplification time is shown in Extended Data Fig. 10d, which shows the results of single-copy reactions run for different times. A detectable signal was observed after a 7-min amplification time. The sensitivity of the FNDs conveys improved LODs in shorter amplification times compared to previous work with RPA using gold nanoparticles^{43–46}. In addition, as a proof-of-concept, a clinical sample (University College London Hospitals (UCLH) clinical standard, 4×10^4 copies per μl) was successfully detected. This involved the addition of an RNA-extraction step (Fig. 4d), which would need to be adapted for point-of-care testing. RPA has been shown to be relatively robust to complex samples, but this remains a major challenge for the field of nucleic acid testing⁴⁷. The positive clinical standard had a mean SBR of around 19 compared to the negative plasma control.

In order to demonstrate the suitability of this system for rapid detection of early disease, a small proof-of-concept experiment was performed using a seroconversion panel of thirteen samples taken over six weeks, spanning the initial stages of an HIV-1 infection. Extended Data Fig. 10e shows that RNA is detected as early as when using the PCR with reverse transcription (RT-PCR) gold standard, giving positive results for six out of seven RT-PCR-positive samples and zero out of six RT-PCR-negative samples. However, this is a preliminary study,

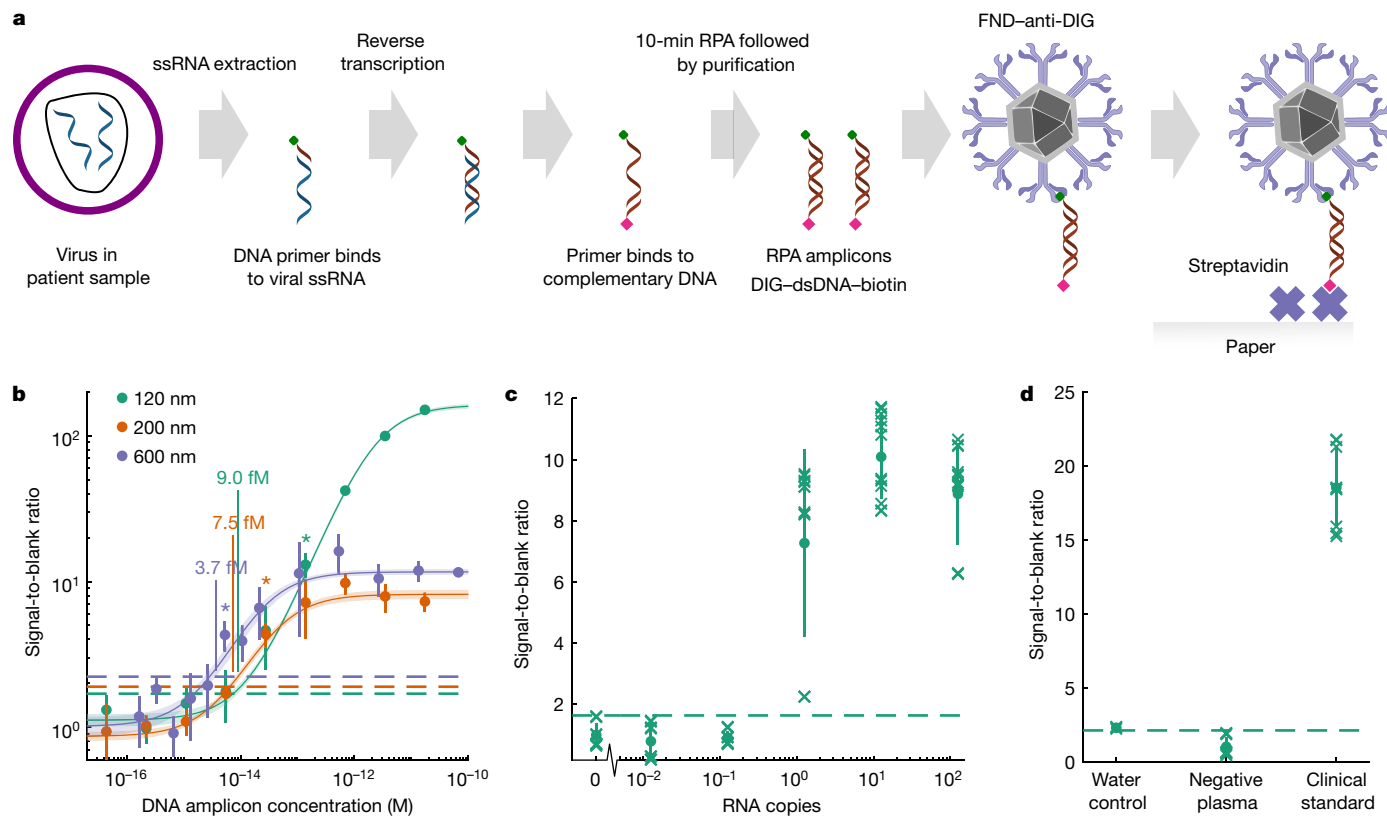


Fig. 4 | Single-copy detection of HIV-1 RNA on LFAs using RT-RPA and FNDs. **a**, A schematic of the assay. Digoxigenin (DIG) and biotin-modified primers were used in a RT-RPA reaction to produce labelled amplicons, which bind to anti-DIG-functionalized FNDs and streptavidin-printed test lines on the LFA strips, forming a sandwich structure in the presence of amplicons. **b**, Dilution series of amplicons were run on LFAs for three different FND sizes (120, 200 and 600 nm). Serial dilutions were plotted (dots showing means with error bars showing s.d., $n = 3-9$ technical replicates, $n = 3$ measurement replicates), and fitted to the Langmuir adsorption model in equation (6) (Methods). Limits of detection for 120, 200 and 600-nm FNDs were 9.0, 7.5 and 3.7 fM respectively. Asterisks mark the lowest concentrations for each particle size that are significantly different from the blanks at the 95% confidence level, calculated

by ANOVA ($P = 10^{-7}$, 10^{-5} and 0.03 from Tukey HSD post hoc test for 120, 200 and 600-nm FNDs, respectively). **c**, Serial dilutions of HIV-1 RNA copies were amplified with RT-RPA (10 min), purified and run on LFAs with 600-nm FNDs. The RNA concentration was plotted against the SBR (data are mean \pm s.d., crosses show individual measurements), with $n = 4$ experimental replicates and $n = 3$ measurement replicates for each sample. Single-copy sensitivity was achieved ($P = 10^{-8}$ from ANOVA from Tukey HSD post hoc test; see Extended Data Fig. 10b, c). **d**, The system was applied to a proof-of-concept positive clinical sample (UCLH clinical standard) and negative human plasma control, giving a mean SBR of around 19 and a P value (comparison between the negative and positive clinical samples) of 8×10^{-13} with a t value of -19.3 from an unpaired one-tailed t -test.

and further optimization with clinical samples and a larger study will be required to precisely ascertain the clinical sensitivity.

Conclusions

Here we demonstrate the use of FNDs as an ultrasensitive fluorescent label for in vitro diagnostic assays, using microwave-based spin manipulation to increase the signal-to-background ratio and therefore the sensitivity. The system was demonstrated in an LFA format with two assays. Using a biotin-avidin model, a fundamental LOD of 0.5 particles per μ l was measured—five orders of magnitude more sensitive than gold nanoparticles—with the caveat of increased cost due to the need for a fluorescence reader (see Supplementary Table 1), but the advantage of enabling the capture of quantitative data (as compared to visual interpretation). By applying FNDs to a sandwich assay for oligonucleotide detection, single-copy sensitivity was achieved for the detection of RNA, using 600-nm FNDs and with a 10-min RT-RPA step. The sensitivity of the FND detection system (LOD of 2,200 copies per μ l with RT-RPA amplicons, measured post-amplification) means that a short amplification time is possible while achieving higher sensitivity than has been previously demonstrated with other nanomaterials^{45,48}, making the test more suitable for point-of-care applications. A comparison with other fluorescence-based amplicon detection on LFAs is

shown in Supplementary Table 2. The system was also demonstrated with HIV-1-positive and -negative clinical samples with the addition of an RNA-extraction step.

The remaining challenges in the translation of this exemplar RNA detection assay towards a rapid point-of-care test that meets the REASSURED criteria³² are summarized in Supplementary Table 3. The incorporation of the amplification step on the LFA strip⁴⁵ is a major challenge, along with sample processing and RNA extraction in resource-limited settings⁴⁷, and removal of the wash step. However, the sensitivity of this transduction technique means that there is leeway for sensitivity reductions while retaining clinical relevance: we have demonstrated single-copy detection with a 10-min RT-RPA step, up to 50-fold greater sensitivity than the World Health Organization viral suppression threshold⁴⁹ of 1,000 copies per ml. This technique is also easily translatable to other assays, for example to amplification methods using modified primers—including existing PCR assays—by changing only the primers; to direct detection by the hybridization of complementary modified probe sequences to a molecular target; or to protein detection in a sandwich assay using modified antibodies. In order to demonstrate this, detection of the HIV-1 capsid protein using FNDs on paper was evaluated (Extended Data Fig. 11), giving a LOD of 120 fM. FNDs are also applicable to a range of other in vitro diagnostic test formats. In addition, owing to the long fluorescence lifetimes of

NV centres⁵⁰ compared to nitrocellulose⁷, time-gated fluorescence measurements could be used to further improve the sensitivity of FND-based LFAs.

The low power consumption (0.25 W microwave power), optical readout and potential portability of this technique render it suitable for ultrasensitive diagnosis and monitoring in low-resource settings, using a portable fluorescence reader or smartphone-based device including microwave modulation. The nature of lock-in readout makes it robust to background light, minimising sensitivity losses when moving from a microscope to such a portable device. FNDs on paper microfluidics offer a sensitive, robust labelling and readout method for in vitro disease diagnostics.

Online content

Any methods, additional references, Nature Research reporting summaries, source data, extended data, supplementary information, acknowledgements, peer review information; details of author contributions and competing interests; and statements of data and code availability are available at <https://doi.org/10.1038/s41586-020-2917-1>.

- Childress, L. & Hanson, R. Diamond NV centers for quantum computing and quantum networks. *MRS Bull.* **38**, 134–138 (2013).
- Mochalin, V. N., Shenderova, O., Ho, D. & Gogotsi, Y. The properties and applications of nanodiamonds. *Nat. Nanotechnol.* **7**, 11–23 (2012).
- Boudou, J.-P. et al. High yield fabrication of fluorescent nanodiamonds. *Nanotechnology* **20**, 235602 (2009).
- Schirhagl, R., Chang, K., Loretz, M. & Degen, C. L. Nitrogen-vacancy centers in diamond: nanoscale sensors for physics and biology. *Annu. Rev. Phys. Chem.* **65**, 83–105 (2014).
- Igarashi, R. et al. Real-time background-free selective imaging of fluorescent nanodiamonds in vivo. *Nano Lett.* **12**, 5726–5732 (2012).
- Leis, J., Martin, P. & Buttsworth, D. Simplified digital lock-in amplifier algorithm. *Electron. Lett.* **48**, 259 (2012).
- Shah, K. G. & Yager, P. Wavelengths and lifetimes of paper autofluorescence: a simple substrate screening process to enhance the sensitivity of fluorescence-based assays in paper. *Anal. Chem.* **89**, 12023–12029 (2017).
- Childress, L. et al. Coherent dynamics of coupled electron and nuclear spin qubits in diamond. *Science* **314**, 281–285 (2006).
- Chang, H.-C., Hsiao, W. W.-W. & Su, M.-C. *Fluorescent Nanodiamonds* Ch. 11 (Wiley, 2018).
- Yu, S. J., Kang, M. W., Chang, H. C., Chen, K. M. & Yu, Y. C. Bright fluorescent nanodiamonds: no photobleaching and low cytotoxicity. *J. Am. Chem. Soc.* **127**, 17604–17605 (2005).
- Shenderova, O. A. & McGuire, G. E. Science and engineering of nanodiamond particle surfaces for biological applications (review). *Biointerphases* **10**, 030802 (2015).
- Chang, Y. R. et al. Mass production and dynamic imaging of fluorescent nanodiamonds. *Nat. Nanotechnol.* **3**, 284–288 (2008).
- Maze, J. R. et al. Nanoscale magnetic sensing with an individual electronic spin in diamond. *Nature* **455**, 644–647 (2008).
- Balasubramanian, G. et al. Nanoscale imaging magnetometry with diamond spins under ambient conditions. *Nature* **455**, 648–651 (2008).
- Tetienne, J. P. et al. Magnetic-field-dependent photodynamics of single NV defects in diamond: An application to qualitative all-optical magnetic imaging. *New J. Phys.* **14**, 103033 (2012).
- Acosta, V. M. et al. Temperature dependence of the nitrogen-vacancy magnetic resonance in diamond. *Phys. Rev. Lett.* **104**, 070801 (2010).
- Hsiao, W. W. W., Hui, Y. Y., Tsai, P. C. & Chang, H. C. Fluorescent nanodiamond: a versatile tool for long-term cell tracking, super-resolution imaging, and nanoscale temperature sensing. *Acc. Chem. Res.* **49**, 400–407 (2016).
- Vaijayanthimala, V. & Chang, H.-C. Functionalized fluorescent nanodiamonds for biomedical applications. *Nanomedicine* **4**, 47–55 (2009).
- Fu, C.-C. et al. Characterization and application of single fluorescent nanodiamonds as cellular biomarkers. *Proc. Natl Acad. Sci. USA* **104**, 727–732 (2007).
- Chang, B. M. et al. Highly fluorescent nanodiamonds protein-functionalized for cell labeling and targeting. *Adv. Funct. Mater.* **23**, 5737–5745 (2013).
- Waddington, D. E. et al. Nanodiamond-enhanced MRI in situ hyperpolarization. *Nat. Commun.* **8**, 15118 (2017).
- Hegyi, A. & Yablonovitch, E. Molecular imaging by optically detected electron spin resonance of nitrogen-vacancies in nanodiamonds. *Nano Lett.* **13**, 1173–1178 (2013).
- Sarkar, S. K. et al. Wide-field in vivo background free imaging by selective magnetic modulation of nanodiamond fluorescence. *Biomed. Opt. Express* **5**, 1190 (2014).
- Chapman, R. & Plakhoitnik, T. Background-free imaging of luminescent nanodiamonds using external magnetic field for contrast enhancement. *Opt. Lett.* **38**, 1847 (2013).
- Doronina-Amitonova, L., Fedotov, I. & Zheltikov, A. Ultrahigh-contrast imaging by temporally modulated stimulated emission depletion. *Opt. Lett.* **40**, 725 (2015).
- Bhutta, Z. A., Sommerfeld, J., Lassi, Z. S., Salam, R. A. & Das, J. K. Global burden, distribution, and interventions for infectious diseases of poverty. *Infect. Dis. Poverty* **3**, 21 (2014).
- Global HIV & AIDS statistics — 2018 fact sheet. <https://www.unaids.org/en/resources/fact-sheet> (UNAIDS, 2018).
- May, M. et al. Impact of late diagnosis and treatment on life expectancy in people with HIV-1: UK Collaborative HIV Cohort (UK CHIC) Study. *Br. Med. J.* **343**, d6016 (2011).
- Gray, E. R. et al. p24 revisited: a landscape review of antigen detection for early HIV diagnosis. *AIDS* **32**, 2089–2102 (2018).
- Price, C. P. Point of care testing. *Br. Med. J.* **322**, 1285–1288 (2001).
- World Malaria Report. <https://www.who.int/malaria/publications/world-malaria-report-2018/en/> (WHO, 2018).
- Land, K. J., Boeras, D. I., Chen, X. S., Ramsay, A. R. & Peeling, R. W. REASSURED diagnostics to inform disease control strategies, strengthen health systems and improve patient outcomes. *Nat. Microbiol.* **4**, 46–54 (2019).
- Walter, J. G. et al. Protein microarrays: reduced autofluorescence and improved LOD. *Eng. Life Sci.* **10**, 103–108 (2010).
- Kim, J. et al. Rapid and background-free detection of avian influenza virus in opaque sample using NIR-to-NIR upconversion nanoparticle-based lateral flow immunoassay platform. *Biosens. Bioelectron.* **112**, 209–215 (2018).
- Paterson, A. S. et al. A low-cost smartphone-based platform for highly sensitive point-of-care testing with persistent luminescent phosphors. *Lab Chip* **17**, 1051–1059 (2017).
- Boudou, J. P., David, M. O., Joshi, V., Eidi, H. & Curmi, P. A. Hyperbranched polyglycerol modified fluorescent nanodiamond for biomedical research. *Diamond Relat. Mater.* **38**, 131–138 (2013).
- Hermanson, G. T. Zero-length crosslinkers. In *Bioconjugate Techniques* 3rd edn (ed. Hermanson, G. T.) Ch. 4 (Academic, 2013).
- González Flecha, F. L. & Levi, V. Determination of the molecular size of BSA by fluorescence anisotropy. *Biochem. Mol. Biol. Educ.* **31**, 319–322 (2003).
- Reth, M. Matching cellular dimensions with molecular sizes. *Nat. Immunol.* **14**, 765–767 (2013).
- Ngom, B., Guo, Y., Wang, X. & Bi, D. Development and application of lateral flow test strip technology for detection of infectious agents and chemical contaminants: a review. *Anal. Bioanal. Chem.* **397**, 1113–1135 (2010).
- Armbruster, D. A. & Pry, T. Limit of blank, limit of detection and limit of quantitation. *Clin. Biochem. Rev.* **29**, S49–S52 (2008).
- Daher, R. K., Stewart, G., Boissinot, M. & Bergeron, M. G. Recombinase polymerase amplification for diagnostic applications. *Clin. Chem.* **62**, 947–958 (2016).
- Lillis, L. et al. Cross-subtype detection of HIV-1 using reverse transcription and recombinase polymerase amplification. *J. Virol. Methods* **230**, 28–35 (2016).
- Crannell, Z. A., Rohman, B. & Richards-Kortum, R. Equipment-free incubation of recombinase polymerase amplification reactions using body heat. *PLoS ONE* **9**, e112146 (2014).
- Rohman, B. A. & Richards-Kortum, R. R. A paper and plastic device for performing recombinase polymerase amplification of HIV DNA. *Lab Chip* **12**, 3082 (2012).
- Boyle, D. S., Lehman, D. A. & Lillis, L. Rapid detection of HIV-1 proviral DNA for early infant diagnosis using rapid detection of HIV-1 proviral DNA for early infant diagnosis. *MBio* **4**, e00135-13 (2013).
- Dineva, M. A., Mahilum-Tapay, L. & Lee, H. Sample preparation: a challenge in the development of point-of-care nucleic acid-based assays for resource-limited settings. *Analyst* **132**, 1193 (2007).
- Jauset-Rubio, M. et al. Ultrasensitive, rapid and inexpensive detection of DNA using paper based lateral flow assay. *Sci. Rep.* **6**, 37732 (2016).
- Phillips, A. et al. Sustainable HIV treatment in Africa through viral-load-informed differentiated care. *Nature* **528**, S68–S76 (2015).
- Kuo, Y., Hsu, T.-Y., Wu, Y.-C., Hsu, J.-H. & Chang, H.-C. Fluorescence lifetime imaging microscopy of nanodiamonds in vivo. In *Proc. Advances in Photonics of Quantum Computing, Memory, and Communication VI* Vol. 8635, 863503 (SPIE, 2013).

Publisher's note Springer Nature remains neutral with regard to jurisdictional claims in published maps and institutional affiliations.

© The Author(s), under exclusive licence to Springer Nature Limited 2020

Methods

Resonator design

CST Studio Suite 2015 (Dassault Systems) was used to create a 3D model of the resonator design, solving Maxwell's equations over a sweep of microwave frequencies to determine reflected and absorbed power. The design was based on copper patterned on a printed circuit board, using Rogers 4003C substrate for low dielectric loss at microwave frequencies. The top side had an interdigitated capacitor and a capacitor-inductor omega-shaped loop, and the bottom had a ground plane. The dimensions of these components were varied iteratively to maximize the absorption at 2.87 GHz and ensure an impedance of 50 Ω for coupling to the frequency generator. The final design was exported as a 2D CAD file.

Preparation of functionalized FNDs

Polyglycerol (PG)-functionalized FNDs were conjugated to antibodies using disuccinimidyl carbonate (DSC) as shown in Extended Data Fig. 3c. DSC activates hydroxyl surface groups to form succinimidyl carbonates, which can then react with antibodies to form stable carbamate or urethane bonds³⁷.

In a typical synthesis, 100 μl FND-PG (1 mg ml⁻¹, Adámas Nanotechnologies, high brightness 120 nm core + 20 nm PG FND NDNV140nmHiPG2mg) were centrifuged at 21,130g for 7.5 min to condense the particles into a pellet. The supernatant was then removed and the FNDs were resuspended in anhydrous *N,N*-dimethylformamide (DMF, 99.8%, Sigma-Aldrich). After resuspension in DMF, the colloidal solution was sonicated for 5 min in an ultrasonic bath. The washing and sonication steps were repeated three times to remove water. After the last centrifugation, the particles were resuspended in 100 μl of a 50 mg ml⁻¹ solution of DSC ($\geq 95\%$, Sigma-Aldrich) in DMF and placed in a thermoshaker for 3.5 h at 300 rpm at room temperature. Excess reagents were removed by three cycles of centrifugation and resuspension in DMF (as described above). After the third centrifugation, the particles were resuspended in 100 μl deionized water.

Depending on the desired surface functionalization, 13.7 μl of anti-DIG antibodies (1 mg ml⁻¹, Abcam, ab76907) or 6.8 μl BSA-biotin (2 mg ml⁻¹ in deionized water, Sigma-Aldrich) were added to the activated FNDs. The mixture was placed in a thermoshaker overnight for 15 h at 300 rpm at room temperature. The remaining succinimidyl carbonates were quenched by adding of 10 μl of Tris-HCl pH 7.5 (1M, Thermo Fisher Scientific). After 30 min, the unbound reagents were removed by three cycles of centrifugation and resuspension in deionized water (100 μl) and stored in 100 μl of PBS with 0.1 wt% BSA.

After functionalization, the FND concentrations were quantified by fluorescence intensity, as this remains unchanged during the functionalization reactions: the fluorescence originates from the atomic structure of the FNDs, so is unaffected by surface modifications. This was carried out by performing a serial dilution of the FND stock solution (of known mass concentration, c_p , of 1 mg ml⁻¹ based on manufacturers specifications) and using a spectrophotometer to measure the fluorescence compared to the functionalized-FND solution. A linear regression was fitted to the fluorescence intensity of the serial dilution of the stock FND solution against FND concentration and interpolated to calculate the mass concentration of the functionalized particles. Examples of this for the three different particle sizes are shown in Extended Data Fig. 5c. This was converted to molar concentration (C_p) using the diameter (d), density of diamond (ρ), and Avogadro constant (N_A), shown in equation (1):

$$C_p(\text{M}) = \frac{c_p(\text{mg ml}^{-1})}{d^3(\text{nm}^3)} \times \frac{10^3}{\frac{\pi}{6} \times \rho(\text{mg nm}^{-3}) \times N_A(\text{mol}^{-1})} \quad (1)$$

Characterization of nanoparticles. Excitation spectra of the FNDs were acquired with a fluorescence microplate reader (SpectraMax i3,

Molecular Devices LLC) and served as a reference to estimate the final FND concentration by comparison of the fluorescence intensity with the stock solution. Emission spectra were recorded with a spectrometer (SPM-002, Photon Control) with a 500-nm LED light source (pE-4000, CoolLED). FTIR spectroscopy was performed by conjugating particles as described above, and storing in deionized water (maximum of 2 days), before centrifuging at 21,130g to condense the particles into a pellet and removing as much supernatant as possible to form a paste. This paste was pipetted onto the spectrometer (Bruker, Alpha). Three measurements of each sample were taken using 16 reads per measurement. Dynamic light scattering data and zeta potentials were measured with a Zetasizer (Zeta Sizer Nanoseries, Malvern Instruments) using a 150-fold dilution of the FNDs. The resulting number plots were fitted to the skewed exponential in equation (2) to find the peak diameter.

$$N(x) = \frac{\exp\left(\frac{-(x-\mu)^2}{2\sigma^2}\right) \text{erfc}\left(\frac{-\alpha(x-\mu)}{\sqrt{2}\sigma}\right)}{\sqrt{2\pi}\sigma} \quad (2)$$

where N is the number fraction, x is the diameter, μ is the mean of the diameter distribution, σ is the standard deviation and α is the skew parameter.

Quantification of antibody binding sites on FND surface

In order to quantify the number of active antibody binding sites on the surface, an assay similar to PCR-ELISA (enzyme-linked immunosorbent assay) and that described in ref.⁵¹ was developed. FNDs (300 μl) were functionalized with anti-DIG antibodies, as described in the section 'Preparation of functionalized FNDs', except the final suspension was in DNase/RNase-free distilled water (Thermo Fisher UltraPure) rather than storage buffer, and the particles were concentrated fivefold (to 5 pM, 60 μl). The suspension was subsequently split in half for a positive sample and a negative control, and 6 μl of a 6 \times running buffer solution was added to each, to a final concentration of 1 \times running buffer (5% milk + 0.05% Empigen in water). A large excess of a DIG-modified DNA sequence (0.9 μM final concentration) was added to the positive sample, and the same excess of the same DNA sequence but with no DIG modification was added to the negative control. A short DNA sequence (82 bp) was used to avoid the bound DNA blocking available sites on the FND surface. The DIG-DNA was left to bind to the FND-antibody for 2 h. After binding, each solution was diluted to 400 μl in DNase/RNase-free distilled water before centrifuging at 376g for 2 min and removing the supernatant. This washing was repeated four times to remove excess DNA, with the final suspension in 150 μl 100 $\mu\text{g ml}^{-1}$ salmon sperm DNA solution (Thermo Fisher UltraPure).

qPCR was then performed on the final suspensions. The template, primers and probe sequences are listed in Extended Data Fig. 8d (assay taken from ref.⁵²). The master mix was the TaqMan Fast Virus 1-Step Master Mix (Thermo Fisher) with primers at 300 nM and the probe at 150 nM, and 4 μl of sample in a total volume of 15 μl . The standard was constructed from serial dilutions of the pHRSIN-CSGW plasmid⁵³. The qPCR was performed by an Applied Biosystems 7500 Real-Time PCR System (Thermo Fisher), and the copy numbers quantified by the 7500 software (v.2.0.6). The FND concentrations in the final suspensions were measured as described in the section 'Preparation of functionalized FNDs'. Dividing the DNA copy number by the FND number gave the number of active binding sites per FND.

Target amplification by recombinase polymerase amplification

RNA template generation. The template was designed using an alignment of 2,929 clinical isolates of HIV-1 from the Los Alamos HIV Sequence Database⁵⁴ to identify conserved areas. The alignment was mapped to the HXB2 (K03455) HIV-1 reference genome using Geneious Software (v.10.0.6) and a highly conserved region of 229 bp (1573-1801 bp from HXB2) selected to design five forward and five reverse primers

to be tested in RPA primer selection. Starting from a R9BALΔEnv plasmid (a gift from G. Towers, University College London), DNA template was produced by polymerase chain reaction amplification of the 1,503 bp template sequence using the Phusion High-Fidelity PCR Kit (New England Biolabs). Primer sequences used are shown in Extended Data Fig. 8d. The thermocycling was performed at 98 °C for 30 s, then 30 cycles of: 98 °C for 10 s, 65 °C for 20 s, 72 °C for 25 s, and a final extension of 72 °C for 10 min. The DNA was then transcribed to RNA using the MEGAscript T7 Transcription Kit (Invitrogen) and purified using MEGAclean Transcription Clean-Up Kit (Invitrogen), following the manufacturer's instructions. The concentration of RNA template was measured via Qubit RNA HS assay kit (Invitrogen) with the Qubit 4 Fluorometer.

RT-RPA reaction (amplicon serial dilution). RT-RPA assay was performed on a 1.5 kb HIV-1 in vitro transcribed RNA template. Optimization of the assay is shown in Extended Data Fig. 8. RT-RPA of the template was performed using TwistAmp Exo Reverse Transcription Kit (TwistDx), following the manufacturer's instructions. The reaction time was 30 min at 37 °C shaking at 200 rpm in an incubator (New Brunswick Innova 42). Nucleic acid sequences are listed in Extended Data Fig. 8d, including a fluorescent probe. During amplification, exonuclease cuts the tetrahydrofuran, releasing the fluorescent tag (FAM) from the quencher, producing a quantitative signal. The resulting RPA products were incubated with RNase A (QIAGEN) for 2 h, before purification of amplified template to remove primers and fragments of RNA using QIAquick PCR Purification Kit (QIAGEN), following the manufacturer's instructions. Quantification by measuring absorption at 260 nm is confounded by RNA contamination, so double-stranded (ds)DNA quantification was performed using a Quant-iT PicoGreen ds-DNA Assay Kit (Invitrogen), following the manufacturer's instructions. Fluorescence measurements were taken with an ultraviolet-visible spectrophotometer (Molecular Devices, SpectraMax i3).

RT-RPA reaction (final assay with amplification). RT-RPA of the template was performed using TwistAmp Basic Kit (TwistDx). The master mix, containing 480 nM of forward and reverse primers (for sequences see Extended Data Fig. 8d, Integrated DNA Technologies), 1× rehydration buffer (TwistDx), reverse transcriptase (M-MLV Reverse Transcriptase, Invitrogen) and nuclease-free water (Invitrogen), was prepared in a tube. For each RPA reaction, 2 µl of target HIV-1 RNA template was added to 45.5 µl of master mix and a freeze-dried RPA pellet. The reaction was started by adding 2.5 µl of magnesium acetate to each reaction, giving a final reaction volume of 50 µl. The RT-RPA reactions proceeded at 37 °C in a thermal incubator for 10 min. The RT-RPA products were purified by QIAquick PCR Purification Kit (QIAGEN) and resuspended in a final volume of 50 µl elution buffer for each reaction.

RT-RPA reaction (UCLH clinical standards). RNA from the UCLH HIV-1 viral load positive and negative standards (personal communication, gift from P. Grant, UCLH) was extracted from a 140 µl sample using the QIAamp Viral RNA Mini Kit (Qiagen) essentially according to the manufacturer's instructions, except that elution was in 60 µl water. Ten microlitres of extracted RNA in water was used for each RT-RPA reaction.

RT-RPA reaction (seroconversion panel). RNA from an HIV-1 seroconversion panel (thirteen samples: ZeptoMetrix Corporation, Panel Donor No. 73698) was extracted from a 140-µl sample using the QIAamp Viral RNA Mini Kit (Qiagen) essentially according to the manufacturer's instructions, except that elution was in 60 µl water. Two microlitres of extracted RNA in water was used for each RT-RPA reaction. The RT-RPA reactions proceeded at 37 °C in a thermal incubator for 10.5 min. The RT-RPA products were purified by QIAquick PCR Purification Kit

(Qiagen) and resuspended in a final volume of 50 µl elution buffer for each reaction.

Lateral flow assay

The following assays all use LFA strips with a poly-streptavidin test line, blocked by a proprietary polyvinylpyrrolidone-sucrose method (Mologic). The strips were 5 mm wide with the test line positioned 7 mm from the bottom of the strip.

A major challenge in developing sensitive LFAs is non-specific binding. To this end, sweeps of running buffers and washing buffers were performed to identify the combination that gave the best SBR (see Extended Data Fig. 6). This gave rise to a reduction in non-specific binding to the strip, reducing the blanks, and increasing the signal in turn. The optimum buffers in this study were found to be non-fat milk 5 wt% + 0.05 vol% Empigen in deionized water (running buffer) and 0.2 wt% BSA with 0.2 vol% Tween 20 in acetate buffer 10 mM pH 5 (washing buffer).

Having chosen running and washing buffers, the background was further reduced by optimising the concentration of FNDs, as shown in Extended Data Fig. 7a, b. LFA strips were run with a dilution series of FND concentration. A positive test (500 pM of DNA) and a negative control (deionized water) were run at each FND concentration. The fitted relationships between positive and negative lock-in amplitude signals and FND concentration were used, along with modelling of equilibrium binding, depending on antigen and FND concentration. This enabled the estimation of the LODs and dynamic ranges at each FND concentration, as explained in Extended Data Fig. 7c, d and Supplementary Information section 2, leading to the selection of the FND concentration. The dynamic range is limited by the total number of FNDs at the top end and the non-specific signal in the negative at the bottom end. The chosen concentration gave a per-strip FND cost of less than 0.02 cents (USD) (4.8 ng of FNDs per strip). The total cost of consumables per test and estimated costs of a strip reader are shown in Supplementary Table 1.

The LFAs were performed by pipetting the solutions to be run into wells of a 96-well plate, then dipping the strips into the wells. All LFAs were performed at room temperature. Purified single-strand (ss)DNA concentrations were measured by absorption using the Nanodrop One^c (Thermo Scientific).

Assay with FND-BSA-biotin. BSA-biotin-functionalized FNDs were diluted in running buffer to the particle concentrations shown in Extended Data Fig. 5d. Then, 55 µl of this suspension was run on each LFA strip.

Assay for model RT-RPA products. The initial optimization and benchmarking was performed using a model ssDNA RT-RPA 'amplicon' (a short ssDNA strand with digoxigenin and biotin modifications at opposite ends), before moving to real RT-RPA amplicons for the final assay. A comparison of real RT-RPA amplicons with the model ssDNA 'amplicon' is shown in Extended Data Fig. 9a, validating its use for optimization, with similar dissociation constant (K_D) values and dynamic ranges, although more variation in the blanks with real amplicons gives a higher LOD. A Monte Carlo simulation of the variances of the clinical sample lock-in amplitudes that can be explained by FND size distribution gives a value of around 8–9% of the total variance (Extended Data Fig. 9d). A further approximately 0.1–2% of variance is explained by periodic drift in the modulation amplitude (Extended Data Fig. 9e), and frequency noise contributes negligible variation (Extended Data Fig. 9f), indicating that the majority is from other factors, such as strip-to-strip inconsistency. This strip-to-strip variation is more evident with larger FNDs, which could be because they are close to the minimum pore size of the nitrocellulose. LODs for the three FND diameters using the model ssDNA 'amplicon' is shown in Extended Data Fig. 9b.

Article

A single strand of DNA (26 bp), functionalized with digoxigenin at the 3' end and biotin at the 5' end (Integrated DNA Technologies, 5' biotin-GTCCGAGCGTACGACGAACGGTCGCT-digoxigenin 3') was used as a model for RT-RPA amplicons produced with biotin and digoxigenin functionalized primers. These model ssDNA strands were diluted in running buffer and 50 μ l of this solution was mixed with 5 μ l of anti-digoxigenin antibody-functionalized FND suspension (1,400, 170 and 3 fM in PBS for 120, 200 and 600 nm diameters, respectively). After 10 min at room temperature, these solutions were run on LFA strips. After all the solution was run (approximately 10 min), the strips were transferred to wells of a 96-well plate with 75 μ l of washing buffer (around 12 min).

Assay for real RT-RPA products (amplicon serial dilution). After purification and quantification of amplicons, the assay was run and washed identically to the model RPA products with FND concentrations of 2,600, 120 and 4 fM for 120, 200 and 600 nm diameters, respectively.

RT-RPA used a digoxigenin-modified forward primer and a biotin-modified reverse primer. The RT-RPA products, therefore, consist of dsDNA (181 bp), each copy including a digoxigenin molecule at one end and a biotin molecule at the other. These modifications bind to anti-digoxigenin-functionalized FNDs and the poly-streptavidin test line on the nitrocellulose paper, respectively, forming a sandwich structure and immobilising FNDs in the presence of amplicons, as shown in Fig. 4a.

Final assay for RNA quantification with RT-RPA. After purification, 10 μ l of 6 \times running buffer (30 wt% non-fat milk with 0.3 vol% Empigen in deionized water) was added to the 50 μ l RT-RPA product. Then, 5 μ l of anti-digoxigenin antibody-functionalized FND suspension was added before running the strips as already described. For the lowest positive sample (average of 1.26 copies), there is a 71% chance of having at least one copy, based on the Poisson distribution. This gives a 26% chance of all four experimental replicates having at least one copy, using the binomial distribution, and a 42% chance for three of the four replicates. For the next dilution (average of 0.13 copies), these probabilities decrease to 0.019% and 0.60%. These probabilities are consistent with the results in Fig. 4.

Fluorescence Modulation and Imaging. The paper strips were imaged using a fluorescence microscope (Olympus BX51) with a 550 nm green LED as excitation light source (pE-4000, CoolLED), with a filter cube containing an excitation filter (500 nm bandpass, 49 nm bandwidth, Semrock), a dichroic mirror (596 nm edge, Semrock) and emission filter (593 nm long-pass, Semrock). A 20 \times /0.4 BD objective (LMPlanFL, Olympus) was used. Images were recorded with a high-speed camera (ORCA-Flash4.0 V3, Hamamatsu) using HCLImage Live software (Hamamatsu).

All strips were measured when dry to eliminate any possible variation due to drying during measuring. Extended Data Fig. 12 shows the detection on wet strips and the effect of drying on the lock-in amplitude of the FND signal. This experiment was performed by running positive and negative LFAs with the model 'amplicon' as above, then fixing each strip to the microscope stage directly after completing the wash step. A 15-s lock-in measurement at an exposure time of 20 ms was taken every 1 min. The light source was only on during measurement to prevent it speeding up drying. One of the negative controls was measured for less than 55 min (35 min), so its mean was used after this time in Extended Data Fig. 12. There is a small loss in sensitivity on wet strips (around 1.4–1.9 times), corresponding to a necessary increase in isothermal amplification time of less than 1 min.

A microwave field was generated by a voltage controlled oscillator (VCO, Mini-Circuits, ZX95-3360+) and a low noise amplifier (Mini-Circuits, ZX60-33LN+) connected to the resonator circuit board

(Minitron, Rogers 4003C 0.8 mm substrate and 1 ozft⁻² (300 g m⁻²) copper weight). The resonator was attached to the microscope stage. The tuning voltage of the VCO was set to maximize the decrease in fluorescence. Modulation of the signal was achieved by modulating the input voltage of the VCO with an on-chip reference frequency generator at 4 Hz using a 32.768 kHz crystal oscillator (DS32KHZ, Farnell) with a 14-stage frequency divider (CD4060BM, Farnell). Circuit board design was performed using EAGLE (Autodesk). A sweep of modulation frequencies was performed using this VCO and amplifier, using a microcontroller (Arduino Nano 3.0) to generate the different modulation frequencies.

The power dependence of the decrease in fluorescence was recorded using a benchtop microwave generator (HM8135, Rohde & Schwartz Hameg) and a low noise amplifier (Mini-Circuits, ZRL-3500+). A broad sweep of microwave frequencies was measured with a radiofrequency signal generator (WindFreak Technologies, SynthUSBII).

Computation lock-in and LOD

The fluorescence signal was modulated with a set modulation frequency (F_m) and the amplitude of the resulting signal was computed with a computational lock-in algorithm. Images were recorded with the high-speed camera (ORCA-Flash4.0 V3, Hamamatsu) at a sampling frequency F_s . Each frame was averaged to get a mean pixel value at each time point $t_0 = 0$ to $t_L = L/F_s$, where L was the total number of frames. A moving average low-pass filter with a span width of $1.5 \times F_s/F_m$ was applied to the fluorescence time series. The filtered signal, V_{in} was multiplied by two reference signals: in-phase ($\sin(2\pi F_m t)$) and $\pi/2$ out-of-phase ($\cos(2\pi F_m t)$) to obtain V_x and V_y , respectively:

$$V_x = V_{in} \times \sin(2\pi F_m t) \quad (3)$$

$$V_y = V_{in} \times \cos(2\pi F_m t) \quad (4)$$

The d.c. components of these two signals, X and Y , were calculated by finding the mean of V_x and V_y , respectively, and enabled the evaluation of the magnitude R of the lock-in amplitude at the frequency F_m according to:

$$R = \sqrt{X^2 + Y^2} \quad (5)$$

Where there was no FND saturation (BSA-biotin assays), the LOD was computed by fitting the lock-in amplitude, as a function of concentration, c , to a linear regression. Where there was saturation, (all assays except BSA-biotin assays), a Langmuir isotherm was fitted:

$$SBR = k_0 + k_1 \times \frac{[T]}{K_D + [T]} \quad (6)$$

where k_0 is SBR of the negative control, k_1 is a scaling constant representing the SBR at target saturation, $[T]$ is the amplicon concentration and K_D is the equilibrium dissociation constant. Fitting was performed in MATLAB using the fitlm and nlinfit functions for linear and Langmuir fits, respectively, weighting the fit by the variance at each concentration.

The LOD was defined as the intersection of the lower 95% confidence bound of the fit with the upper 95% confidence bound of the blank measurements⁴¹.

Data availability

The datasets generated during and/or analysed during the current study, and the computer code used are available from the corresponding author on reasonable request, in line with the requirements of UCL and the funder (EPSRC policy framework on research data).

51. Kim, E. Y. et al. A real-time PCR-based method for determining the surface coverage of thiol-capped oligonucleotides bound onto gold nanoparticles. *Nucleic Acids Res.* **34**, e54 (2006).
52. Besnier, C., Takeuchi, Y. & Towers, G. Restriction of lentivirus in monkeys. *Proc. Natl Acad. Sci. USA* **99**, 11920–11925 (2002).
53. Bainbridge, J. W. et al. In vivo gene transfer to the mouse eye using an HIV-based lentiviral vector; efficient long-term transduction of cornealendothelium and retinal pigment epithelium. *Gene Ther.* **8**, 1665–1668 (2001).
54. Foley, B. et al. HIV Sequence Compendium 2017. LA-UR-18-25673 (Los Alamos National Laboratory, 2018).
55. Kong, J. & Yu, S. Fourier transform infrared spectroscopic analysis of protein secondary structures. *Acta Biochim. Biophys. Sin. (Shanghai)* **39**, 549–559 (2007).
56. Zadeh, J. N. et al. NUPACK: Analysis and design of nucleic acid systems. *J. Comput. Chem.* **32**, 170–173 (2011).
57. SantaLucia, J. A unified view of polymer, dumbbell, and oligonucleotide DNA nearest-neighbor thermodynamics. *Proc. Natl Acad. Sci. USA* **95**, 1460–1465 (1998).
58. Laitinen, M. P. & Vuento, M. Affinity immunosensor for milk progesterone: Identification of critical parameters. *Biosens. Bioelectron.* **11**, 1207–1214 (1996).

Acknowledgements We thank M. Schormans for help with circuit design, M. Thomas for assistance with dynamic light scattering measurements and M. Towner for assistance with FTIR measurements. This work was funded by the i-sense EPSRC IRC in Early Warning Sensing Systems for Infectious Diseases (EP/K031953/1); i-sense EPSRC IRC in Agile Early Warning Sensing Systems in Infectious Diseases and Antimicrobial Resistance (EP/R00529X/1); the National Institute for Health Research University College London Hospitals Biomedical Research Centre; Royal Society Wolfson Research Merit Award to R.A.M. (WM130111); LCN

Departmental Studentship to B.S.M.; EPSRC Centre for Doctoral Training in Delivering Quantum Technologies to G.D. (EP/L015242/1); H2020 European Research Council Local quantum operations achieved through the motion of spins to J.J.L.M. (771493); and the UCLH NHS Foundation Trust to J.H. and E.N.

Author contributions B.S.M. and R.A.M. conceived the research and led the study; P.J.D. advised on nanodiamonds and J.J.L.M. on microwave modulation. B.S.M. demonstrated the initial proof-of-concept; B.S.M. and L.B. designed and optimized the lock-in analysis, functionalization and LFA design; B.S.M., L.B. and D.H. performed all the FND LFA experiments; H.D.G. designed, optimized and performed RT-RPA assays including primer design and template generation; D.H. adapted and performed RT-RPA assays and purification; J.J.L.M. and G.D. designed the microwave delivery including resonators; E.R.G. performed clinical RNA extraction, and advised on virology including primer design; J.H. performed qPCR on the seroconversion panel; E.N. provided clinical expertise; B.S.M. and E.R.G. designed and performed binding-site quantification experiments; B.S.M., L.B. and R.A.M. drafted the manuscript; and all authors reviewed and revised the manuscript.

Competing interests B.S.M., L.B., G.D., P.J.D., J.J.L.M. and R.A.M. are inventors on the UK patent application number 1814532.6 filed by University College London Business.

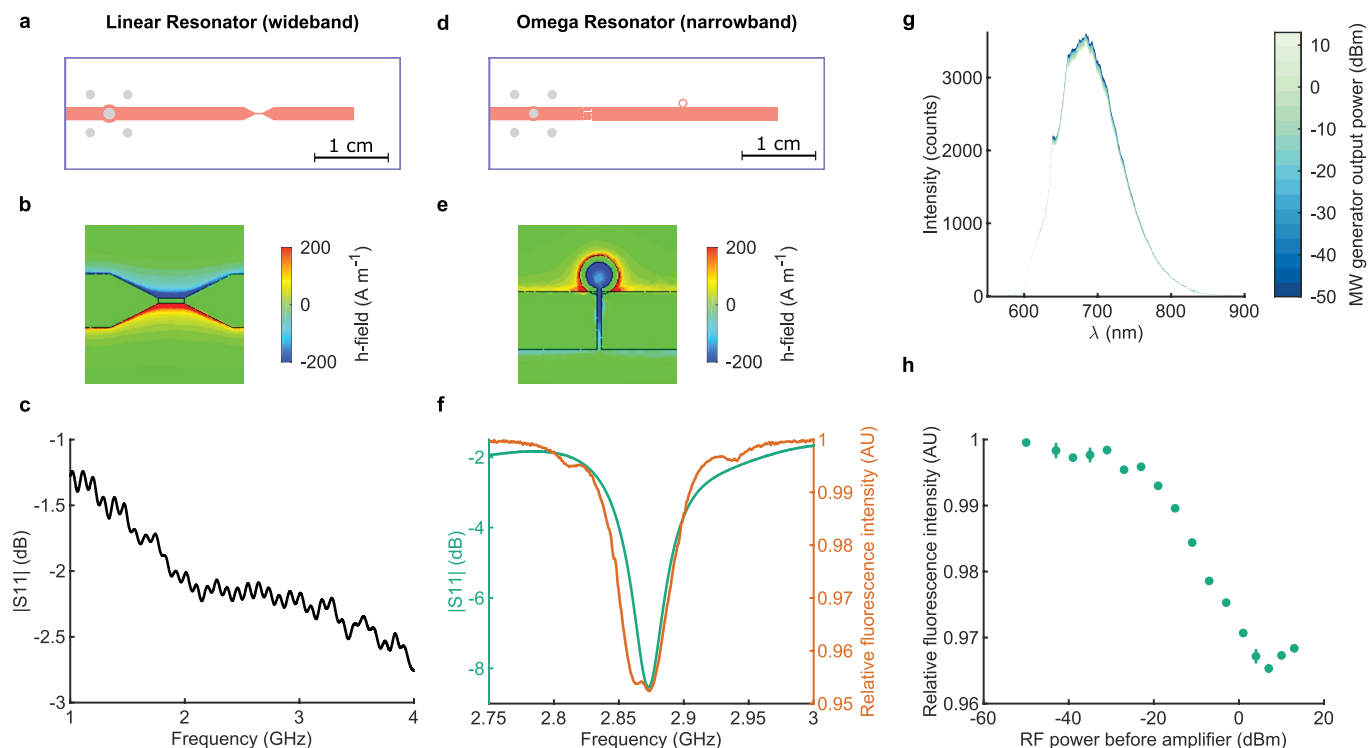
Additional information

Supplementary information is available for this paper at <https://doi.org/10.1038/s41586-020-2917-1>.

Correspondence and requests for materials should be addressed to B.S.M. or R.A.M.

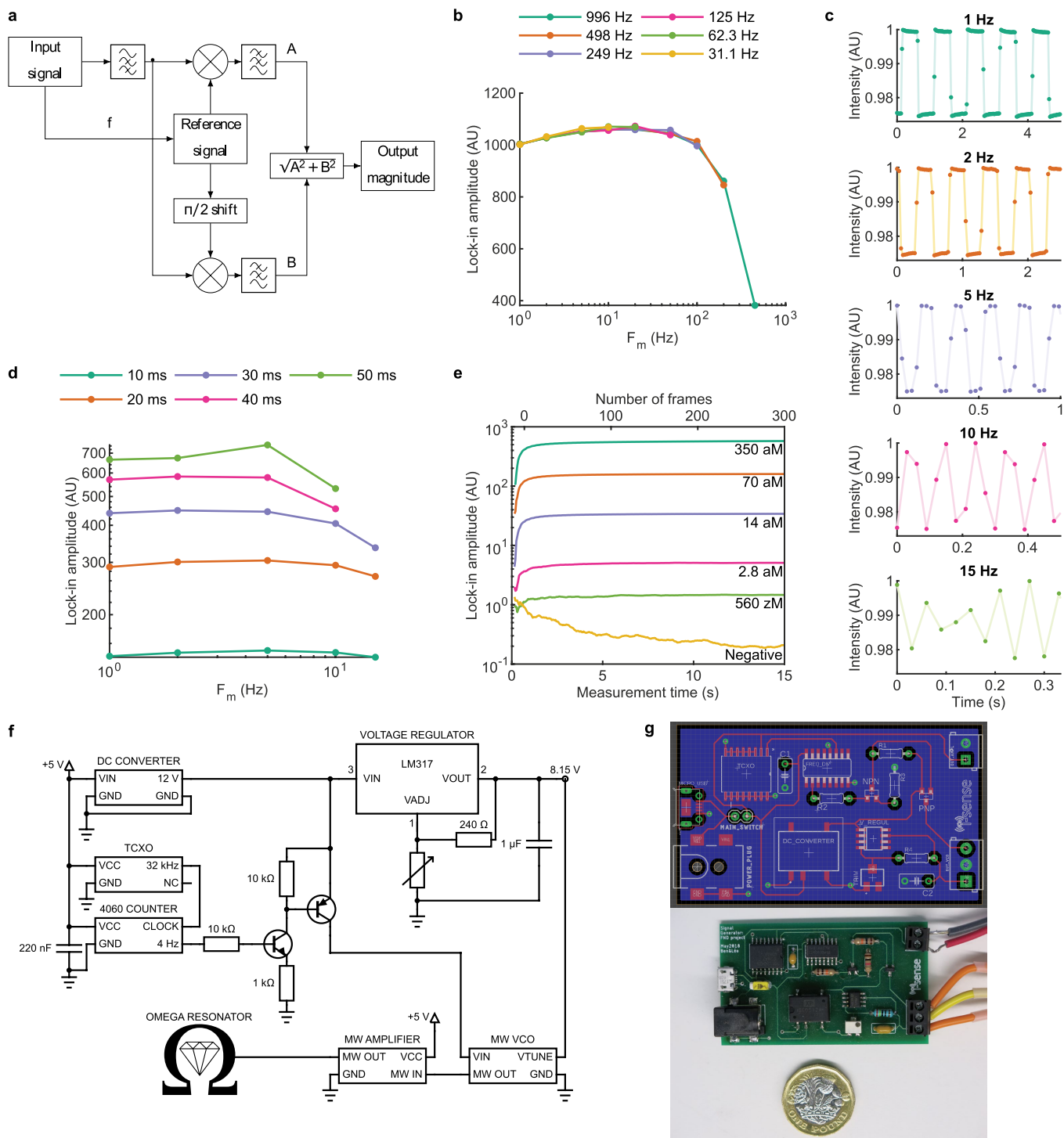
Peer review information *Nature* thanks Takuya Segawa and the other, anonymous, reviewer(s) for their contribution to the peer review of this work.

Reprints and permissions information is available at <http://www.nature.com/reprints>.



Extended Data Fig. 1 | Optimization of microwave modulation. **a–f**, A linear resonator was designed to have a wideband response over the range 1–4 GHz, and an omega narrowband resonator was designed to have a stronger, narrower resonance at 2.87 GHz with quality factor $Q=100$. The schematic printed circuit board layouts for the two resonators are shown in **a** and **d**, respectively. The resulting simulated fields are shown in **b** and **e**, respectively. The reflected power (S11) is plotted against frequency in **c** and **f**. The narrowband resonator shows 5–6 orders of magnitude greater absorption than the wideband resonator at 2.87 GHz, indicating resonant coupling giving strong absorption. Panel **f** also shows the corresponding FND intensity dip. **g**, Emission spectra of FNDs acted on by a 2.87

GHz microwave field. The powers listed in decibel-milliwatts are the output power of the microwave generator (before the 17 dB amplifier). **h**, Each spectrum is integrated over the whole wavelength range to give a total intensity, which is plotted against preamplifier power. This shows a linear relationship between fluorescence intensity and microwave power (in dBm) above a threshold power, and up to 7 dBm, where the amplifier reaches its 1 dB compression power. At this point, the fluorescence starts to increase again owing to a loss in the quality of the sinusoid leading to power lost in harmonics. Dots show means and error bars show the s.d., with $n=3$ measurement repeats.

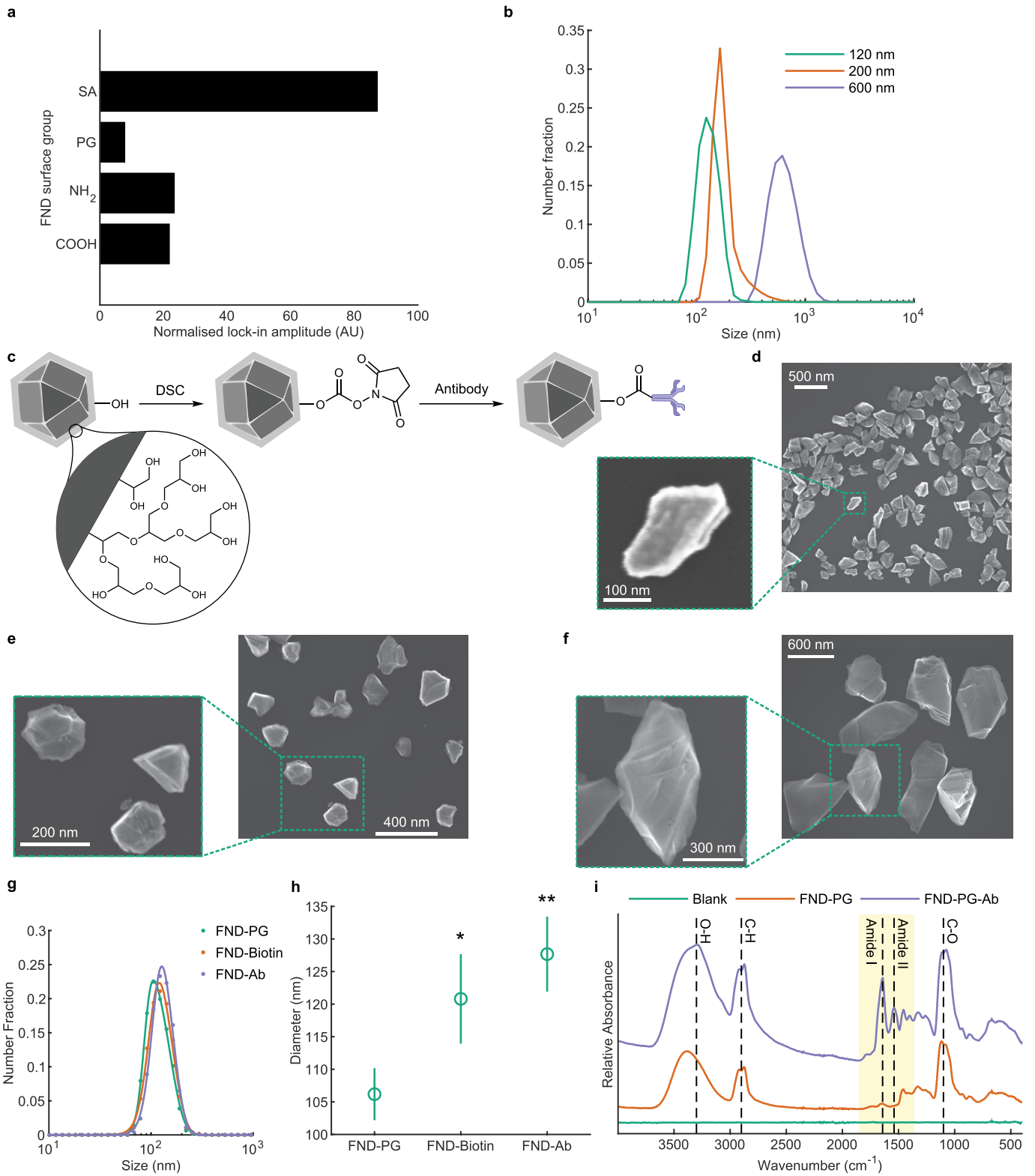


Extended Data Fig. 2 | See next page for caption.

Article

Extended Data Fig. 2 | Optimization of lock-in analysis. **a**, Schematic of the computational lock-in algorithm used to extract the microwave modulated FND signal from the background. The input signal is high-pass filtered using a moving average filter to remove low-frequency drift. It is subsequently multiplied by cosine and sine functions with frequency F_m , and the resulting signals are low-pass filtered to generate the in phase and quadrature components, respectively, of the vector representation of the signal. The magnitude of this vector is calculated to remove the effect of phase, giving the output magnitude. **b**, The variation of lock-in amplitude with modulation rate (F_m) at various sampling rates (F_s). A single strip with very high intensity was modulated at F_m values between 1–450 Hz, and sampled at various F_s values between 3.89–996 Hz. The resulting plot shows that lock-in amplitude is independent of F_s when $F_s > 2F_m$. **c**, **d**, The relationships between lock-in amplitude, exposure time (T_e) and modulation frequency (F_m). An identical LFA strip was measured with exposure times between 10–50 ms, using the maximum possible F_s for each T_e , and F_m values between 1–15 Hz. **d** shows F_m against lock-in amplitude at various exposure times. It is shown that the lock-in amplitude has its maximum at around 5 Hz for all frequencies, and reduces when F_m is close to $F_s/2$, its maximum possible value. This is evident in the raw signal plots in **c** for each F_m at a fixed exposure time of 30 ms. As F_m approaches $F_s/2$, the sampling effects obscure the square wave, decreasing lock-in amplitude. For maximum lock-in amplitude, the highest

possible T_e should be used. Here, we are limited to 50 ms by the background autofluorescence of the nitrocellulose, which saturates the camera above this value. A corresponding F_m of 4 Hz was chosen as it is in the optimal range and is a power of 2, so can be achieved by simply dividing the temperature compensation crystal oscillator (TCXO) frequency. **e**, The variation of lock-in amplitude with total measurement time at $F_m = 4$ Hz and $F_s = 20$ Hz for five different concentrations of FNDs and a negative control, immobilized with a biotin–avidin interaction. The positive amplitudes stabilize quickly, reaching 5% of their 15 s value in 3.9 s for positive results. The negative results take longer to stabilize, reaching 5% of their 15 s value in 13 s. A measurement time of 15 s (300 frames) was used for subsequent measurements. **f**, Schematic circuit design of temperature compensation crystal oscillator (TCXO)-based modulated microwave source. It is powered by a 5 V source which powers a TCXO, which outputs a 32.768 kHz square wave. This is converted to a 4 Hz signal by a 4060 counter chip. This square wave controls two transistors which deliver 12 V stepped up power (d.c. converter) to the microwave VCO. The bias voltage is regulated from 12 V to 8.15 V by a voltage regulator. The VCO microwave output is amplified by the MW amplifier and transmitted to the omega resonator. **g**, Printed circuit board layout of the prototype (65 mm × 38 mm). Outputs for the microwave amplifier and microwave VCO are at the top right and bottom right, respectively. A photo of the printed circuit board with a £1 coin (GBP) for scale is shown below.

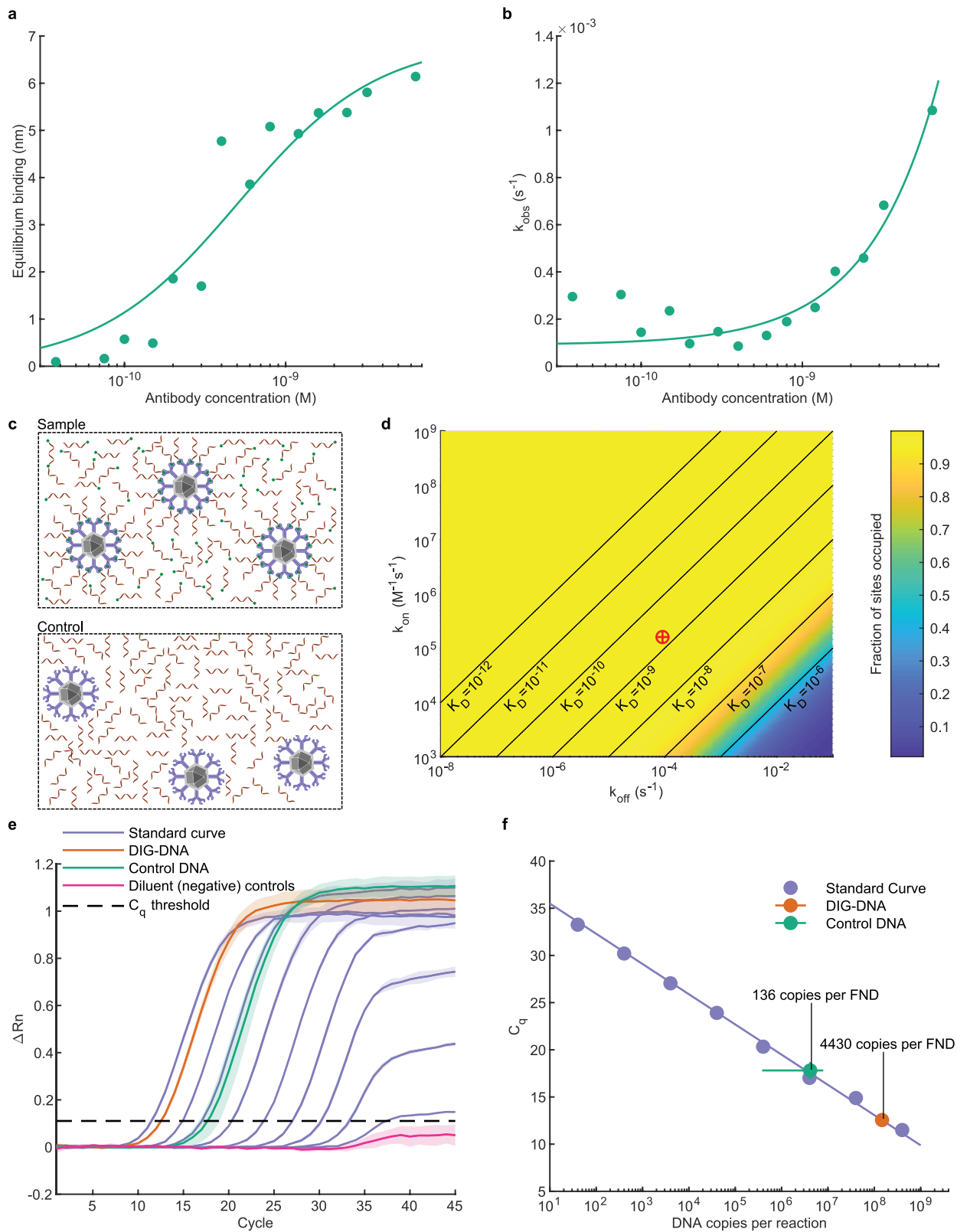


Extended Data Fig. 3 | See next page for caption.

Extended Data Fig. 3 | FND characterization and functionalization.

a, Comparison of the non-specific binding of various commercial FNDs with various surface functionalizations on LFAs. The lock-in amplitude at the test line was measured to quantify non-specific binding. The LFAs were also pre-blocked with a polyvinylpyrrolidone-sucrose solution (proprietary method, Mologic). The lowest non-specific binding was from the PG-functionalized particles (FND-PG), as the PG adds a hydrophilic layer. **b**, Dynamic light scattering of three different FND particle core diameters: 120, 200 and 600 nm. **c**, A schematic of antibody functionalization of FND-PG. DSC activates hydroxyl surface groups to form succinimidyl carbonates, which can then react with antibodies to form stable carbamate or urethane bonds. **d-f**, Scanning electron microscope images of FNDs with particle core diameters of 120, 200 and 600 nm, respectively. **g**, Dynamic light scattering was also used to measure the size and aggregated fraction after functionalization of 120 nm FND-PG before and after functionalization with BSA-biotin or antibodies. Dots show the means of $n = 3$

measurement replicates. Fitting the number plots to skew exponentials (equation (3), plotted as lines) gave peak particle hydrodynamic diameters of 106, 121 and 128 nm. **h**, The fitted peak diameters are plotted with error bars denoting their 95% confidence intervals ($n = 3$ measurement replicates), showing no significant difference between the bio-functionalized diameters (FND-biotin, FND-antibody), but both are significantly different from the pre-functionalization diameter (FND-PG): $*P \leq 0.05$; $**P \leq 0.01$, ANOVA with Tukey HSD post hoc test. **i**, FTIR spectroscopy of FND-PG and antibody-functionalized FND-PG. Lines show means of $n = 6$ measurement replicates for FND samples and $n = 2$ measurement replicates for the blank. C-O and C-H peaks, indicative of the PG layer, can be seen in both FND-PG and FND-PG-antibody at around $1,100 \text{ cm}^{-1}$ and at around $2,900 \text{ cm}^{-1}$, respectively. The FND-PG-antibody spectrum displays additional peaks at around $1,640 \text{ cm}^{-1}$ and at around $1,540 \text{ cm}^{-1}$, suggesting protein amide I and amide II bonds, respectively⁵⁵, showing that protein functionalization was successful.



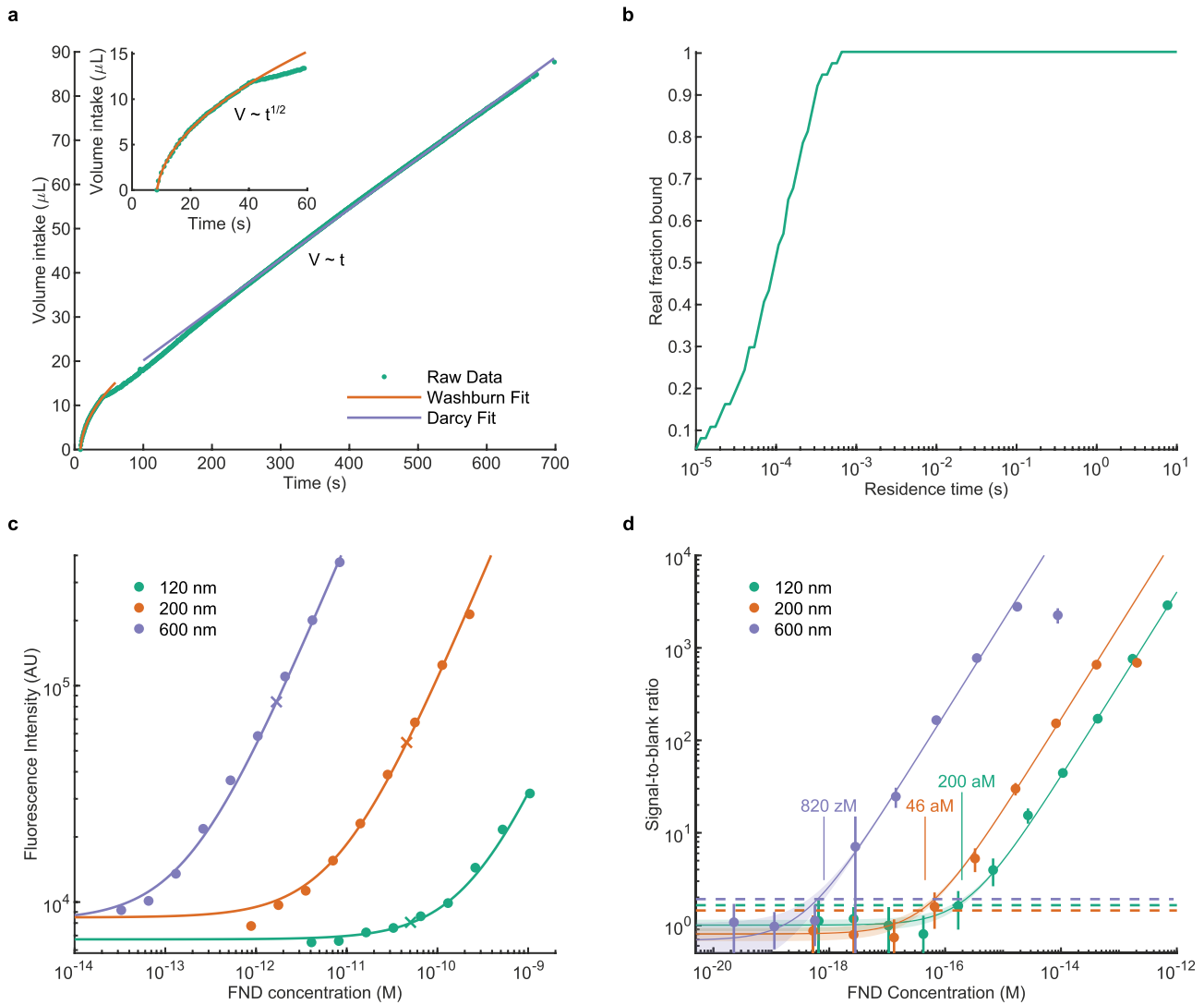
Extended Data Fig. 4 | See next page for caption.

Article

Extended Data Fig. 4 | Quantification of the number of available binding sites per FND.

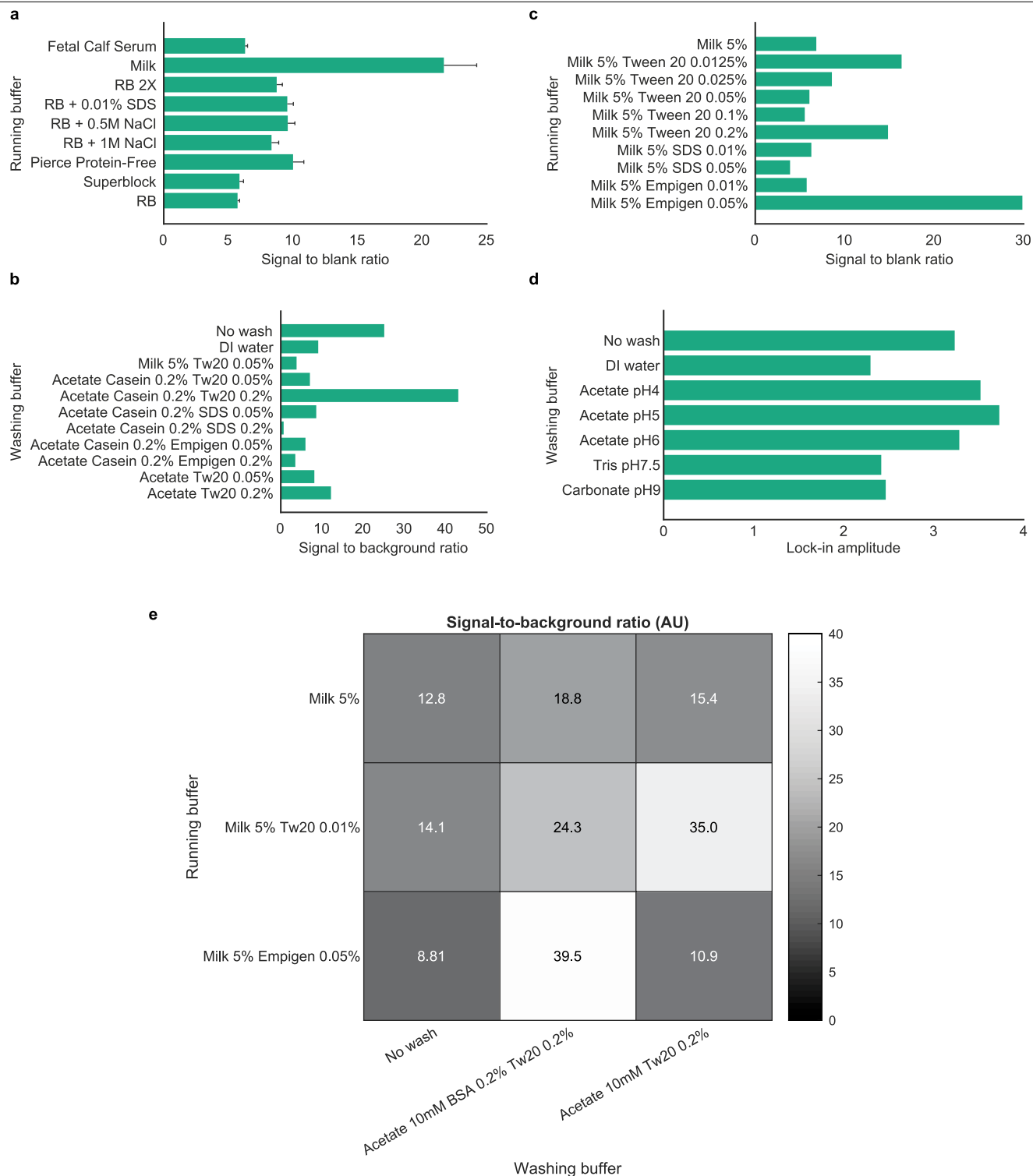
a. Initially, binding constants of the anti-DIG antibody binding to DIG were measured using interferometry. Full experimental details are shown in Supplementary Information section 1. Binding at different concentrations was measured and the resulting curves were fitted to exponentials. To find the equilibrium dissociation constant (K_D), equilibrium binding values, B , were plotted here against concentration, C . A Langmuir adsorption isotherm was fitted ($B^\infty = \frac{a \times C}{K_D + C}$) giving a K_D value of 5.1×10^{-10} M. **b.** In order to find the on- and off-rates, k_{on} and k_{off} , the observed reaction rates, k_{obs} , at each concentration were plotted and fitted to the linear relationship: $k_{obs} = k_{off} + C \times k_{on}$. The resulting fitted values are $k_{on} = 1.6 \times 10^5 \text{ M}^{-1} \text{ s}^{-1}$ and $k_{off} = 9.1 \times 10^{-3} \text{ s}^{-1}$. **c.** A schematic of the assay to quantify the number of available binding sites per FND. After functionalization of FNDs with anti-DIG antibodies, an approximately 50-fold excess of DIG-modified DNA was added and left to bind for 2 h. The negative DNA control used the same sequence, but with no DIG modification to compensate for non-specific binding and adequate washing. After multiple washes by centrifugation to remove the excess DNA, the remaining DNA (bound to FNDs) was quantified by qPCR. See Extended Data Fig. 8d for template, primer and probe sequences, and Methods for full experimental details. **d.** A kinetic binding simulation was performed to verify that all available sites would be occupied after 2 h with the above excess. The graph shows the fraction of sites on the FNDs which are occupied, with this approximately 50-fold excess, over a range of K_D , k_{on} and k_{off} values. The red cross

in circle marks the location of the anti-DIG antibody used in this paper (using the values measured in **a** and **b**), indicating that more than 99.9% of available sites will be occupied after 2 h. This means that quantifying the DNA gives a true measure of available binding sites. **e.** Amplification plot showing the normalized fluorescence intensity against the number of cycles. A standard curve of each decade from 40 copies to 4×10^8 copies is plotted, along with the sample and negative control FND samples described above. The negative diluent controls are also plotted along with the C_q threshold. The lines show means and shaded areas show the s.d. of repeats ($n = 3$ technical replicates for standard curve, and $n = 6$ for samples). **f.** The resulting C_q values are plotted against copy number per reaction. Dots show means and error bars show s.d. ($n = 3$ technical replicates for standard curve and $n = 6$ for samples). The standard curve was fitted to a logarithmic curve ($C_q = -3.2 \log_{10} \text{copies} + 39$), enabling calculation of the number of copies in the DIG-DNA sample and negative DNA control. Dividing by the particle concentration (measured as shown in Extended Data Fig. 5c) and subtracting the negative DNA control value gives the number of available binding sites per particle as 4,300 sites. This is within what is geometrically plausible, giving an area per antibody of at least 200 nm^2 (assuming at least 1 paratope available of at least 75% of the bound antibodies). The corresponding calculated values for 120 and 200 nm particles are 172 and 477 available binding sites per FND respectively, assuming the same loading density.



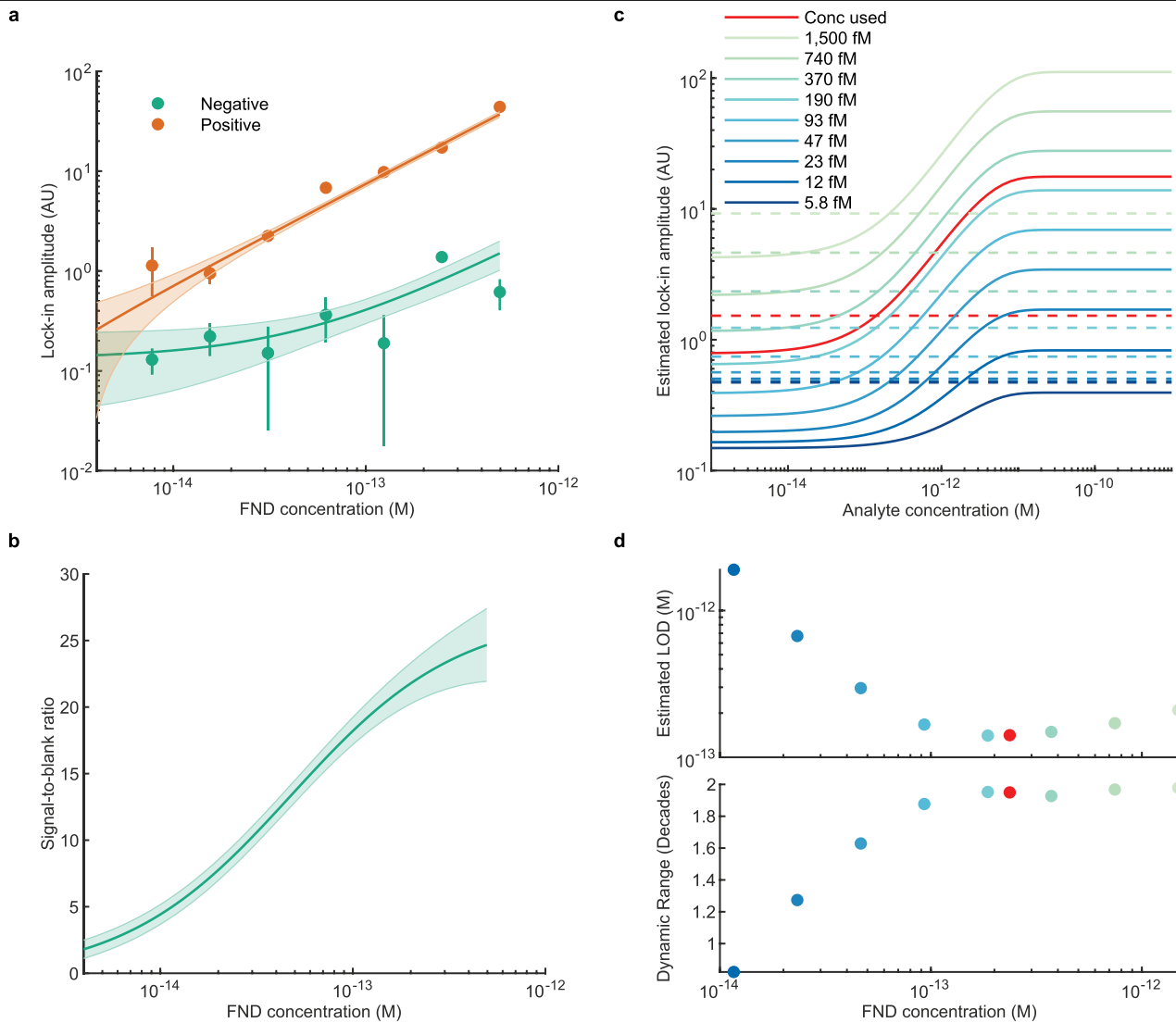
Extended Data Fig. 5 | Lateral flow and FND benchmarking. **a**, Measurement of flow rate of lateral flow strips. During wetting, the flow follows the Washburn equation, where $V \sim t^{1/2}$ (inset), and during fully-wetted flow, Darcy's law for capillary flow is followed ($V \sim t$), with a constant flow rate of $6.9 \mu\text{L min}^{-1}$. **b**, Using a one-to-one receptor–ligand binding approximation, the binding of biotinylated FNDs to streptavidin was modelled kinetically, indicating that all the FNDs bind with a residency time of more than about 10^{-3} s. Here, the residency time is measured as 4 s, using the flow rate from **a**, so all the FNDs should bind. **c**, An example of the measurement of FND concentration. FND fluorescence is unaffected by surface chemistry, so is used to quantify concentration. A serial dilution of FND suspensions from a known stock concentration was performed (dots showing means with error bars showing s.d., $n = 6$ measurement replicates). This was then fitted with a linear regression (lines) to find a relationship between fluorescence intensity and concentration. After each FND functionalization,

the fluorescence intensities of the final suspensions were measured, and the linear fit was used to estimate concentration (crosses). **d**, Fundamental LODs for different sized FNDs on LFAs, using a model biotin–avidin interaction. Suspensions ($55 \mu\text{L}$) of BSA–biotin-functionalized FNDs were run at different concentrations on poly–streptavidin strips. Concentrations were chosen to span the dynamic range of the camera, limited by over-exposure, as seen with the top concentration of 200 and 600 nm FNDs. Dots show means and error bars show s.d. ($n = 3$ technical replicates, $n = 3$ measurement replicates). Each series is fitted to a simple linear regression, shown as the solid line, with 95% confidence intervals shown shaded. LODs for 120, 200 and 600 nm diameter FNDs are 200 aM, 46 aM, and 820 zM respectively, defined by the intersection of the lower 95% confidence intervals of the linear fit with the upper 95% confidence intervals of the blanks for each particle size.



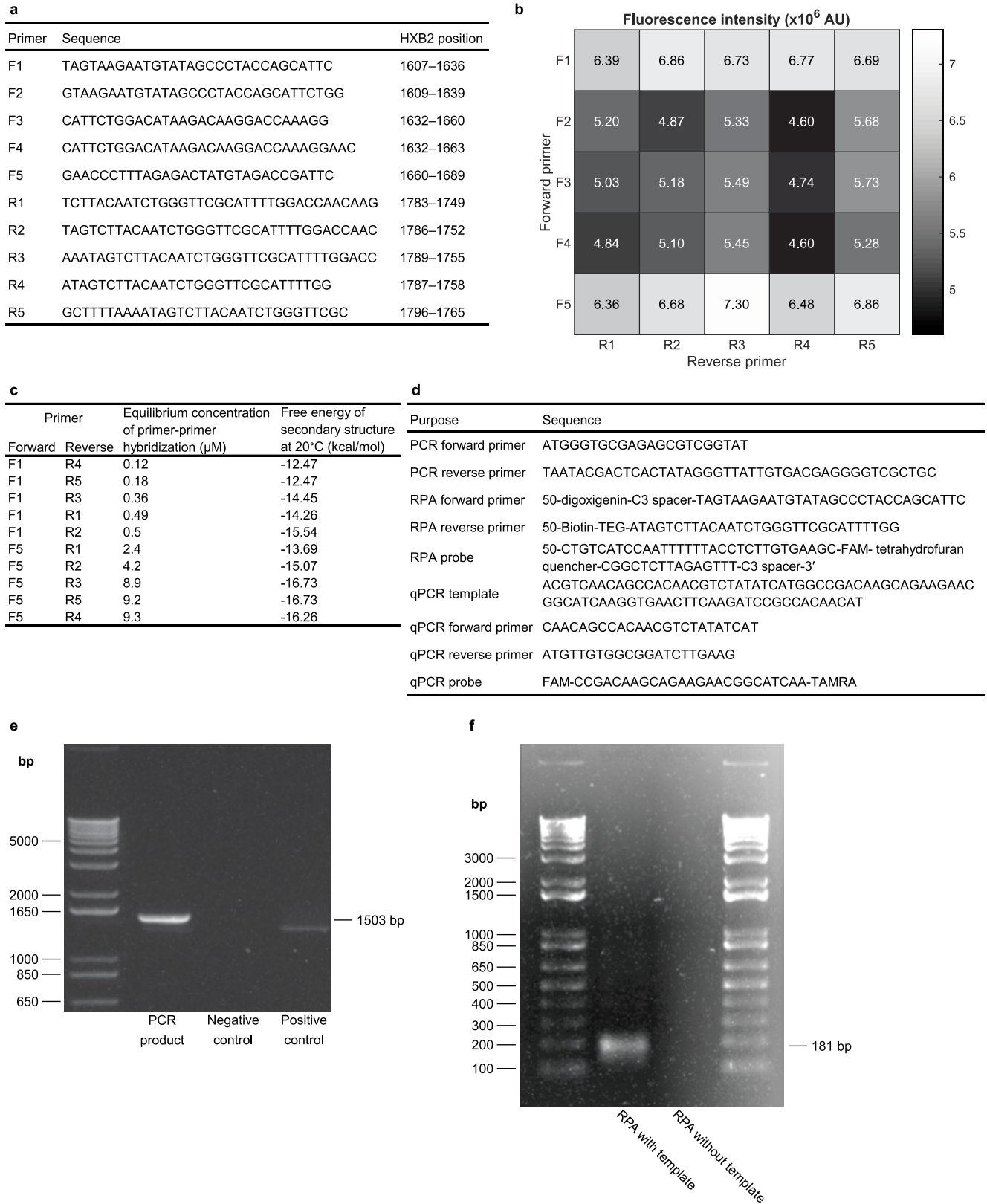
Extended Data Fig. 6 | Assay optimization by buffer selection. Sensitivity is limited by the non-specific binding of FNDs at the LFA test line. LFA strip blocking, running buffer and washing step are, therefore, key factors in improving LOD. In this section 120 nm FNDs were used for optimization. **a**, Signal-to-background comparison for the FNDs in different running buffers. There is no wash step. Error bars show s.d. ($n = 3$ measurement replicates). Milk was selected as the basis for the running buffer. **b**, Subsequently, a sweep of different surfactants was performed ($n = 1$ measurement replicate). The best signal-to-background ratio came from adding 0.05 vol% Empigen, showing a significant increase in the signal-to-background. There is no wash step. **c-e**, The best running buffer was then used for a washing buffer pH sweep ($n = 1$ measurement replicate) (**c**). All washing buffers were run at a volume of 75

μ l, chosen because preliminary experiments showed it to be a good compromise between assay time and washing success. Although results were similar, pH 5 gave the best signal-to-background ratio, so acetate buffer at 10 mM pH 5 was used as the basis for a second washing buffer sweep, shown in (**d**), testing a number of detergents and adding casein at 0.2 wt% as a blocking protein ($n = 1$ measurement replicate). As a final test, the three best running buffers were tested, each with the three best washing conditions, displayed as a grid in (**e**). Each square is the average of three measurements ($n = 3$ measurement replicates). The results were consistent with previous sweeps, the combination of the best running buffer and best washing buffer giving the best signal-to-background. Milk and protein percentages are by weight and detergent percentages are by volume.



Extended Data Fig. 7 | Optimization of FND concentration. The background was reduced by optimising the particle concentration, shown here for 120-nm FNDs. **a**, A positive LFA strip (500 pM of ssDNA) and a negative control (deionized water) were run at varying FND concentrations between 3.88 fM and 496 fM, plotted against FND concentration, and fitted to simple linear regressions. The dots show means and error bars show the s.d. of repeat measurements ($n = 3$ measurement replicates). Linear regressions are shown by solid lines, and shaded areas show the 95% confidence intervals of the fits. **b**, Signal-to-background ratio, found by dividing the fitted linear regressions in **a**, is plotted against FND concentration. At higher concentrations, where the gradient term of the linear regression dominates, the positive and negative lock-in values tend to a constant separation on the log-log plot, so the signal-to-background ratio tends to a constant value of around 27. At low

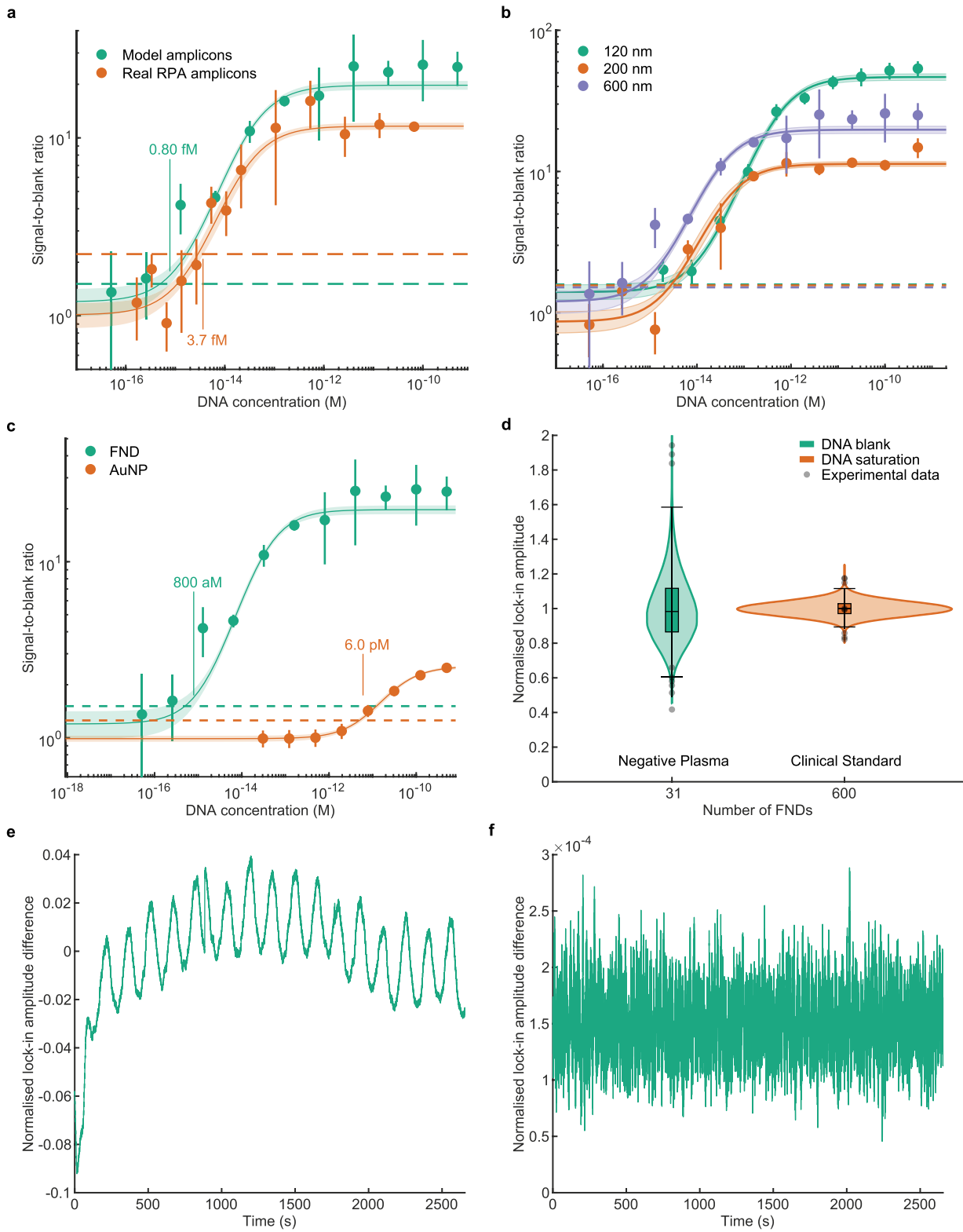
concentrations, the positive and negative curves converge as the negative lock-in amplitude levels off at the noise threshold, and the signal-to-background ratio tends to 1. **c**, The fitted linear regressions in **a** were used, along with the antibody equilibrium dissociation constant measured in Extended Data Fig. 4, to estimate the variation of lock-in amplitude with analyte concentration at different FND concentrations. The principles and equations are described in full in Supplementary Information section 2. The LOD for each FND concentration is defined as the intersection of this plot with the value of the blank plus two times the 95% confidence interval at that value, assuming a low concentration positive would have a similar confidence interval. **d**, The estimated LODs and dynamic ranges from **c**, plotted against FND concentration, to determine the optimum.



Extended Data Fig. 8 | See next page for caption.

Extended Data Fig. 8 | Primer optimization. **a.** List of forward primers (F1–F5) and reverse primers (R1–R5) tested for the initial primer screen. **b.** An initial primer screen was performed to achieve the highest amplification efficiency ($n = 3$ technical replicates) using the TwistAmp Exo Reverse Transcription Kit (TwistDx). The yield of each primer combination was measured by the fluorescence of the exo probe with a fluorescence microplate reader (SpectraMax i3, Molecular Devices LLC). Primers F5 and R3 gave the highest yield, although all the yields were above 63% of this value. **c.** Interactions between forward primers and reverse primers to predict the minimum free energy structures for the ten primer combinations that gave the largest yield of RPA product in the primer screen. The table shows the results of simulations in NUPACK⁵⁶, using an input of 10 μM for each oligonucleotide. The minimum free

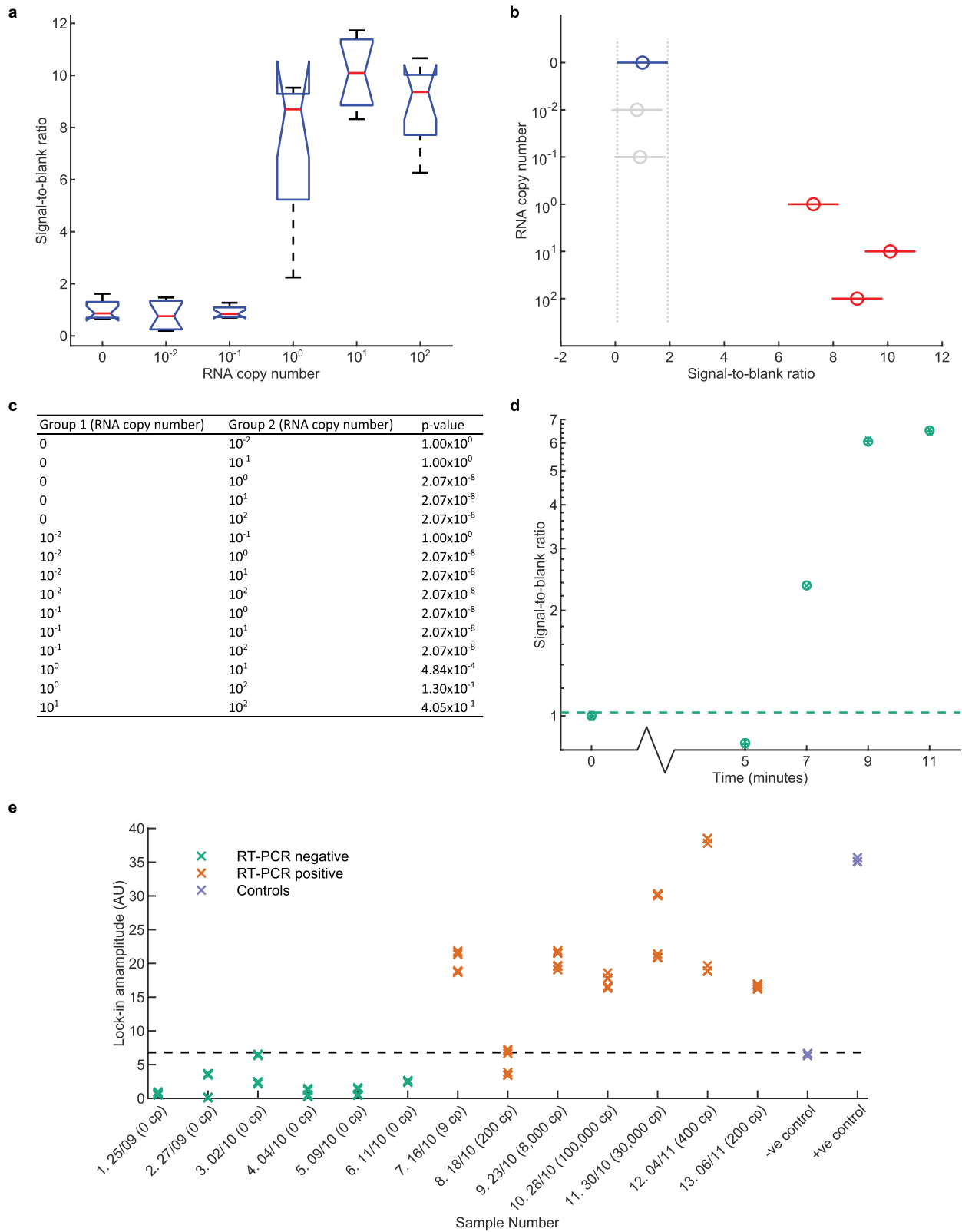
energy secondary structures are the most energetically favourable secondary structures that can be assumed for oligonucleotides of a given primary sequence, calculated using the nearest-neighbour method⁵⁷. Primers F1 and R4 were selected for future work since the energetics of their hybridization are much less favourable than that of F3 and R5, yet they still gave a high RPA yield in the primer screen (93% of the highest yield pair). **d.** A list of oligonucleotides used for PCR, RPA and qPCR assays. The PCR reverse primer included a T7 promoter for RNA transcription (underlined) and a spacer (**bold**). **e.** Gel electrophoresis of 1,503 bp template sequence produced by PCR using a 1% agarose gel. **f.** Gel electrophoresis of 181 bp double-stranded RT–RPA products using a 1% agarose gel.



Extended Data Fig. 9 | See next page for caption.

Extended Data Fig. 9 | Comparison of LODs of model ssDNA with real RPA amplicons and gold nanoparticles. **a**, The dilution series of the real RPA amplicons and the model ssDNA 'amplicons' were plotted against concentration for 600 nm FNDs (dots showing means with error bars showing s.d., $n = 3$ –9 technical replicates, $n = 3$ measurement replicates) with their respective linear fits (solid lines with 95% confidence intervals of the fit shown shaded). The curves are similar, with fitted K_D values of 29 and 22 fM for model and real amplicons, respectively, and similar dynamic ranges. The real amplicons showed increased variation in the blanks, leading to a higher blank cutoff giving a higher LOD, and slightly reduced signal-to-blank ratio. **b**, The dilution series of model ssDNA 'amplicons' were plotted against concentration for 120, 200 and 600 nm FNDs (dots showing means with error bars showing s.d., $n = 3$ technical replicates, $n = 3$ measurement replicates) with their respective linear fits (solid lines with 95% confidence intervals of the fit shown shaded). The LODs are 3.7, 3.6 and 0.8 fM respectively. **c**, Comparison of 600 nm FNDs with 40 nm gold nanoparticles on LFAs, often used in LFAs owing to a good compromise between stability (and therefore ease of functionalization), and sensitivity⁵⁸. Serial dilutions are plotted (dots showing means with error

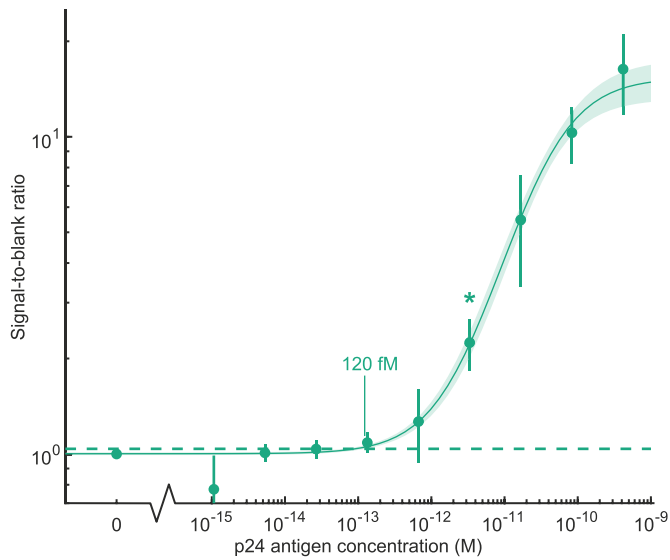
bars showing s.d., $n = 3$ technical replicates, $n = 3$ measurement replicates for the FNDs; and dots with error bars showing the s.d. across the test line, $n = 1$ technical replicate, $n = 1$ measurement replicate for the gold nanoparticles). LODs are calculated as previously, giving 800 aM and 6.0 pM, respectively. **d, e**, A Monte Carlo simulation of the signal variation that can be explained by the FND size distribution (from DLS measurements in Extended Data Fig. 3b) was performed ($n = 200,000$). The violin plots (**d**) show the normalized simulated random variation in lock-in amplitudes due to the 600-nm FND size distribution in the clinical sample assays in Fig. 4d (negative plasma control and clinical standard). The experimental data are overlaid, showing that FND size distribution explains approximately 8–9% of the total experimental signal variance. Full details of the simulation are given in Supplementary Information section 3. A further approximately 0.1–2% of the variance is explained by periodic drift in modulation amplitude, shown over 45 min in **e**, normalized to the mean. **f**, A plot of the variation in lock-in amplitude due to small changes in the modulation frequency, F_m . The variance of the frequency is $3 \times 10^{-8}\%$ over the same period, giving negligible differences in lock-in amplitude.



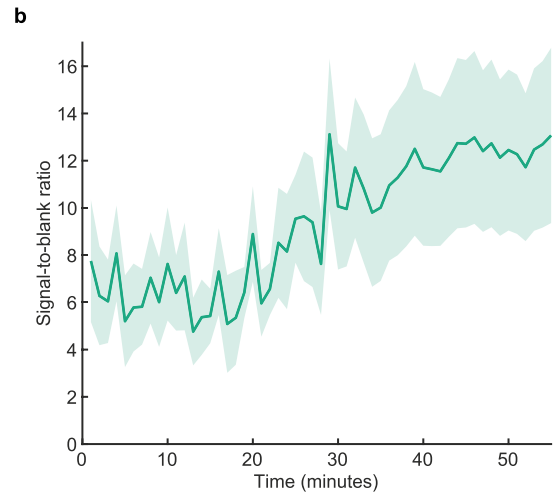
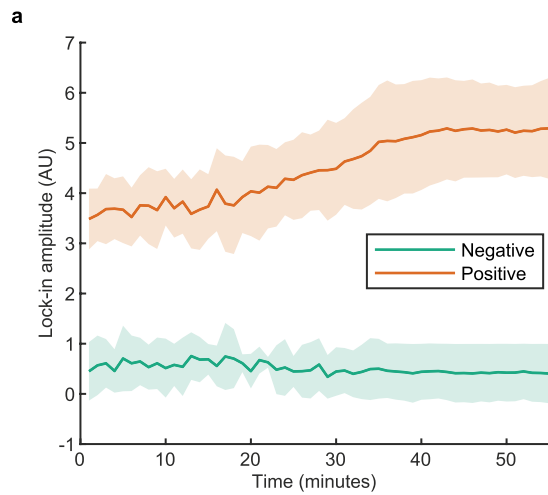
Extended Data Fig. 10 | See next page for caption.

Extended Data Fig. 10 | Further analysis of RT-RPA samples. **a**, ANOVA analysis was performed on the measured lock-in amplitudes of the FND LFAs, giving a P value of 7.4×10^{-29} and F value of 95.6, with 71 total degrees of freedom. Box plots of the data groups are shown (grouped by RNA concentration). The horizontal red lines represent the medians, the horizontal blue lines represent the 25th and 75th percentiles and the notches represent the 95% confidence intervals of the medians. The black dashed lines represent the range for each group. **b**, A graphical comparison of the means of the groups (grouped by RNA concentration). The circles represent the means, and the horizontal lines represent the comparison intervals of the means from Tukey HSD post hoc test (overlap of these intervals denotes statistical similarity). The negative control, highlighted in blue, is shown to be not significantly different from the 10^{-2} and 10^{-1} RNA copy number samples (P values > 0.999 , shown in grey), but it is significantly different from the 1 , 10^1 and 10^2 RNA copy number samples (P values $\approx 10^{-8}$, shown in red). **c**, A table of ANOVA P values. The P value for the null hypothesis that the difference between the means of the two groups is zero. **d**, Comparison of amplification time for a low copy number RT-RPA sample (average of 1.26 RNA copies). Multiple RPA reactions were run and

stopped after different times, before adding to FND LFAs, as described in Methods. A negative control is shown for comparison, and the dashed line represents the upper 95% confidence interval of the negative control. Dots show the mean of $n = 3$ measurement replicates, crosses show the individual measurements, and error bars represent the s.d. **e**, Early disease detection using FND LFAs was demonstrated by a seroconversion panel (ZeptoMetrix Corporation, Panel Donor No. 73698), taken from a single donor over a period of six weeks spanning the early stages of an HIV-1 infection. The thirteen samples of the panel were measured on FND LFAs ($n = 1-2$ experimental replicates, $n = 3$ measurement replicates). The measured values are plotted along with positive and negative non-amplification controls. They are colour-coded for RT-PCR results, and labelled with sample numbers, dates, and copy numbers in brackets. The blank cutoff is defined as the upper 95% interval of the negative control. The results show that the RNA was detectable on FND LFAs as early as RT-PCR, and six out of seven RT-PCR-positive samples were detected on FND LFAs, while six out of six RT-PCR-negative samples were negative.



Extended Data Fig. 11 | Detection of HIV-1 capsid protein on using 600 nm FNDs. A serial dilution of the capsid protein was detected on streptavidin-modified LFAs using a sandwich of a biotinylated capture nanobody and antibody-modified FNDs. The results are plotted ($n = 3-4$ experimental replicates, $n = 3$ measurement replicates), normalized to the blanks for each sample set with dots showing means and error bars showing s.d. These data were then fitted to a Langmuir curve (equation (6), shown as a line with shaded area denoting the 95% confidence interval of the fit). This gives a LOD of 120 fM, and a lowest concentration that is significantly different from the blank (at the 95% confidence level) of 3 pM, marked with *. Full experimental details are shown in Supplementary Information section 4.



Extended Data Fig. 12 | Effect of lateral flow test strip drying on lock-in amplitude of FND assay. **a**, Positive and negative lateral flow test strips were measured over time after running was complete (time = 0), showing a small increase in the positive strip lock-in amplitude as the strip dries (the initial lock-in amplitude is around 70% of the final value); however, no increase is seen

in the negative control. The shaded areas show the standard deviation between repeats ($n=3$ technical replicates). **b**, The resulting signal-to-blank ratio variation over time. The shaded areas show the standard deviation between repeats ($n=3$ technical replicates), showing that the effect of drying is quite small compared to strip-to-strip variation.